

Current Sensor FTC Method for MPTC of Three-Phase Induction Motor Drives without Speed Measurement

Soroush Aghili (s.aghili@sutech.ac.ir)

Independent Sector https://orcid.org/0000-0002-2384-4172

Meisam Noori

Shiraz University of Technology

Adel Khoshdel

Shiraz University of Technology

Ashraf ALI KHAN

Memorial University of Newfoundland

Research Article

Keywords: current sensor fault-tolerant control, encoderless control, flux linkage observer, model reference adaptive system, three-phase induction motor

Posted Date: August 19th, 2022

DOI: https://doi.org/10.21203/rs.3.rs-975600/v1

License: © 1 This work is licensed under a Creative Commons Attribution 4.0 International License.

Read Full License

Current Sensor FTC Method for MPTC of Three-Phase Induction Motor Drives without Speed Measurement

Soroush Aghili¹, Meisam Noori², Adel Khoshdel², Ashraf Ali Khan³

¹Independent Researcher, Alumni of Shiraz University of Technology, Shiraz, Iran.

²Department of Electrical and Electronics Engineering, Shiraz University of Technology, Shiraz, Iran.

³Department of Electrical and Computer Engineering, Faculty of Engineering and Applied Science, Memorial University of Newfoundland, St. John's, NL, Canada.

Correspondence

Soroush Aghili, Department of Electrical and Electronics Engineering, Shiraz University of Technology, Shiraz, Iran.

Email: s.aghili@sutech.ac.ir

Abstract: In encoderless Model Predictive Torque Control (MPTC) of three-phase Induction Motor (IM) drives, current sensors can face different electrical or mechanical faults in harsh industrial environments. In this research, single-phase current sensor Fault-Tolerant Control (FTC) method for MPTC of three-phase IM drives without speed measurement using a flux linkage observer and Model Reference Adaptive System (MRAS) algorithm is proposed. In the presented FTC method, Third-Difference (TD) operators, logic circuit module, flux linkage observer, and MRAS algorithm are utilized for fault detection, fault isolation, estimation of stator currents and fluxes, and speed estimation, respectively. In comparison with the conventional current sensor FTC methods, the proposed method can be utilized for encoderless three-phase IM drives. In order to confirm the usefulness and possibility of the proposed encoderless FTC method, experimental studies are performed for a 0.75 kW three-phase IM drive system in different situations. The achieved results demonstrate good performances of the proposed technique during both normal and faulty situations.

KEYWORKS: current sensor fault-tolerant control; encoderless control; flux linkage observer; model reference adaptive system; three-phase induction motor

NOMENCLATURE

$$i_{as}, i_{bs}, i_{cs}$$
 Stator line currents

$$\psi_{ds}, \psi_{qs}, \psi_{dr}, \psi_{qr}$$

$$i_{ds}, i_{as}, i_{dr}, i_{ar}$$
 Stator and rotor fluxes and currents

$$r_s, r_r$$
 Stator and rotor resistances

$$L_{ls}, L_{lr}, L_{ms}$$

 L_{mr}, L_{s}, L_{r} Stator and rotor leakage, magnetizing, and self-inductances

$$\Omega_r, \Omega_e$$
 Motor speed, angular speed of the rotational reference frame

$$\tau_e, \tau_l$$
 Electromagnetic and load torques

$$\lambda_{\psi}$$
 Weighting factor

$$|\psi_s|, |\psi_r|$$
 Stator and rotor flux amplitudes

$$\Psi_{dm}, \Psi_{qm}$$
 Mutual fluxes

$$\Delta, \Delta^2, \Delta^3$$
 First-, second-, and third-difference operators

$$T_s$$
 Sampling time

1. INTRODUCTION

Three-phase Induction Motor (IM) drives are broadly utilized in various industries such as renewable energy conversion systems, pumps, and electric traction [1-3]. Commonly, speed sensors such as encoder or tachometer are used for high-performance control of three-phase IM drives. The use of speed sensor increases

the cost of drive system and decreases its reliability. Consequently, speed estimation techniques such as Extended Kalman Filter (EKF), Sliding Mode Observer (SMO), signal injection techniques, etc. have become a hot research subject in the field of three-phase IM drive systems [4-8].

Model Predictive Torque Control (MPTC) strategy is a recent alternative control technique to Direct Torque Control (DTC) and vector control. In this strategy, the switching states of the inverter are optimized using a cost function. In recent years, different MPTC techniques have been proposed for three-phase IM drives. For example, Habibullah and Lu proposed an encoderless MPTC method using two EKF algorithms [9]. The obtained results in [9] show that the current distortion can be decreased particularly at low speed region. Zhou et al proposed a control strategy based on MPTC technique using four-switch inverter with suppression of the DC-link voltage offset [10]. Bindal and Kaur introduced a developed MPTC method for three-phase IM drives using fuzzy logic to reduce torque ripples [11]. Feedback correction-based dual reference frame MPTC strategy for encoderless control of three-phase IM drive systems to decrease the electromagnetic torque prediction error was presented by Yan et al [12]. Bhowate et al presented a MPTC with online weighting factor computation [13].

A drive system may suffer from electrical or mechanical fault(s), causing safety and dependability difficulties. In other words, Fault-Tolerant Control (FTC) strategies are highly important for motor drive systems [14-25]. Generally, FTC strategies can be classified into passive FTC systems and active FTC systems. In spite of the simple structure of a passive FTC system, this approach has less fault-tolerant capabilities [14]. In this case active FTC systems are preferable.

Single-phase Current Sensor Faults (CSFs) are common in industrial environment due to electrical, thermal, and mechanical stresses. Failure in current sensors can degrade the drive system performance or in some cases can cause the system shutdown. Current sensor FTC strategies are an important field of study for motor drives.

Although different FTC systems have been developed for three-phase motor drives under current sensor failure, there are few current sensor FTC schemes for encoderless three-phase drives. Compared with the previously published papers, the study on encoderless control of three-phase IM drives under single-phase CSF is relatively mature, and an acceptable performance without speed measurement can be achieved.

In this paper, single-phase current sensor FTC strategy for encoderless MPTC of three-phase IM drives using flux linkage observer and Model Reference Adaptive System (MRAS) algorithm is proposed. In the proposed FTC strategy, a Third-Difference (TD) mechanism, flux linkage observer, and MRAS algorithm are utilized for fault detection, estimation of stator currents, and speed estimation, respectively. Through the flux linkage observer, not only the motor currents but also the stator and rotor fluxes used in the control system are estimated. In the presented system, a logic circuit module executes the task of CSF isolation. In other words, in the proposed scheme a sensorless modified MPTC with a flux linkage observer is used for the healthy IM. After the CSF, the fault detection and isolation units which are based on the TD algorithm and a logic circuit module recognize the CSF condition and select the suitable currents. Then, these currents in cooperation with stator voltages produce the motor speed and fluxes. The motor speed and fluxes are used in the MPTC system. The proposed FTC scheme not only works during the CSF, its performance during normal condition is highly satisfactory as a modified MPTC strategy is used in this condition. According to the previous works in literature, the following contributions can be presented:

- A modified sensorless MPTC for three-phase IM drives under healthy condition using MRAS algorithm is presented.
- A current sensor FTC method for MPTC of three-phase induction motor drives without speed measurement is presented.
- The motor speed, rotor fluxes, stator fluxes, and motor currents using MRAS algorithm and a flux linkage observer are estimated.
- A fault detection and isolation mechanism for the CSF using TD operators and a simple logic circuit module is presented.

Such FTC system can be used in many industrial safety crucial applications such as electric vehicles, ventilation systems, aerospace, transportation systems, etc. The suggested FTC scheme is experimented under different operating conditions using the TMS320F28335 controller board to demonstrate the applicability of the introduced FTC algorithm.

2. LITERATURE REVIEW

Generally, active FTC systems include two main parts: (1) fault detection and isolation systems and (2) a control technique for post-fault operation. This section includes two sections. First, different fault detection and isolation systems for motor drives are discussed. Then, some important works to control motor drives during the CSF are presented.

Fault detection is an important section of active FTC systems. In general, fault detection mechanisms can be categorized into four approaches [26,27]: (1) model-based techniques, (2) signal-based techniques, (3) data-driven techniques, and (4) combinations of (1), (2), and (3). Model-based fault detection strategy is an effective approach which is used in many applications [15-18,22]. In [15,16], artificial neural network and fuzzy logic strategies for the CSF detection were used, respectively. The strategies used in these papers need a large volume of historical information and prior data. Yu et al used a model-based CSF detection method using three separate observers [17]. These observers can monitor the condition of the sensors in the healthy situation. After CSF, these observers detect the faulty condition. Chakraborty and Verma presented a CSF detection technique using Clarke transformations [18]. In [18], two Clarke transformation matrices were utilized to compare the stator current residual with the predefined threshold to determine the faulty situation. Using three observers in [17] and using different Clarke transformation matrices in [18] increase the complexity of the control system structure. Manohar and Das used a CSF detection mechanism based on the TD operator for IM drives [22]. This mechanism can provide fast and effective fault detection even for a slight change in the stator current.

Another essential part of the FTC system is the post-fault control system. There are two possibilities for post-fault control of IM drives under CSF. In the first approach, when the sensor fault happens, the drive system switches from a closed-loop system to an open-loop system [19] or a current sensorless closed-loop control system [20]. This approach reduces drive system performances conspicuously, and it is not appropriate for many industrial applications. In the second approach, an estimation technique is utilized to acquire the faulty current value. It can be mentioned that in this approach, the structure of the control system remains unchanged. In the second technique, the estimated motor current corresponding to the faulty motor current sensor is utilized in the control system. Consequently, uninterrupted and continuous operation can be realized. Different estimation techniques have been presented in the literature to obtain the value of the faulty current during the post-fault operation. Some of these techniques are reviewed as follows: Yu et al used three independent adaptive observers for the post-fault control [17]. These observers provide the estimated current value. As mentioned before, this strategy suffers from high complexity due to three observers. In Chakraborty and Verma, the motor currents were reconstructed using the vector rotator concept [18]. In this paper, the motor currents were estimated based on the actual and command stator currents. Thus, the estimated motor currents change slower than the actual currents in transient states. In Lu et al, a method was proposed for motor current rebuilding without utilizing null

switching conditions [21]. This strategy was applied to an encoderless synchronous motor drive. In [21] the faulty current was estimated using the DC-link current sensor and switching table. In the paper mentioned above, the reconstructed motor currents were used for high-frequency voltage injection-based rotor position estimation. In Manohar and Das, a flux estimator was employed to estimate the currents in DTC of a three-phase IM drive system under CSF [22]. However, this method needs a speed sensor for the estimation of the motor currents. In addition, DTC technique suffers from high torque ripples during low speed region. In [23], the IM currents were estimated using an EKF during post-fault operation. Although EKF is a good choice to estimate the motor currents in the presence of noises, this algorithm increases the computational burden. The used strategy in [23] also requires a position sensor which increases the drive system cost. In Zhang et al, the reconstruction of the faulty currents was performed based on SMO and the current space vector error projection [24]. This strategy was applied to an encoderless control of a synchronous motor. In [25], a simplified current tracing mechanism was proposed to estimate the currents of a three-phase synchronous motor after CSF based on the sinusoidal features of current. In [28], an adaptive observer with estimation of the stator and rotor resistances was proposed for three-phase IM drive systems via one current sensor. Nevertheless, the presented system in [28] does not discuss the control method reconfiguration. In [29], a coupled FTC was proposed for a primary permanent-magnet linear machine. In this paper, by coupling the faulty mover with the healthy mover, the presented controller can control the faulty mover, in which current sensors fail. In [30], an encoderless current sensor FTC strategy with the SMO was proposed. However, this method suffers from slow dynamics due to several PI controllers and chattering problems due to the SMO.

3. PROPOSED CURRENT SENSOR FTC SCHEME

In three-phase IM drive systems, current sensors are frequently prone to fault(s) [22]. Thus, in order to increase the dependability and safety of three-phase IM drives, FTC of these motors under CSF is critical and vital, especially for some critical industrial applications such as aerospace. In this section, the suggested scheme for current sensor FTC of IM drives is presented. Figure 1 illustrates the proposed current sensor FTC method for the encoderless three-phase IM drive.

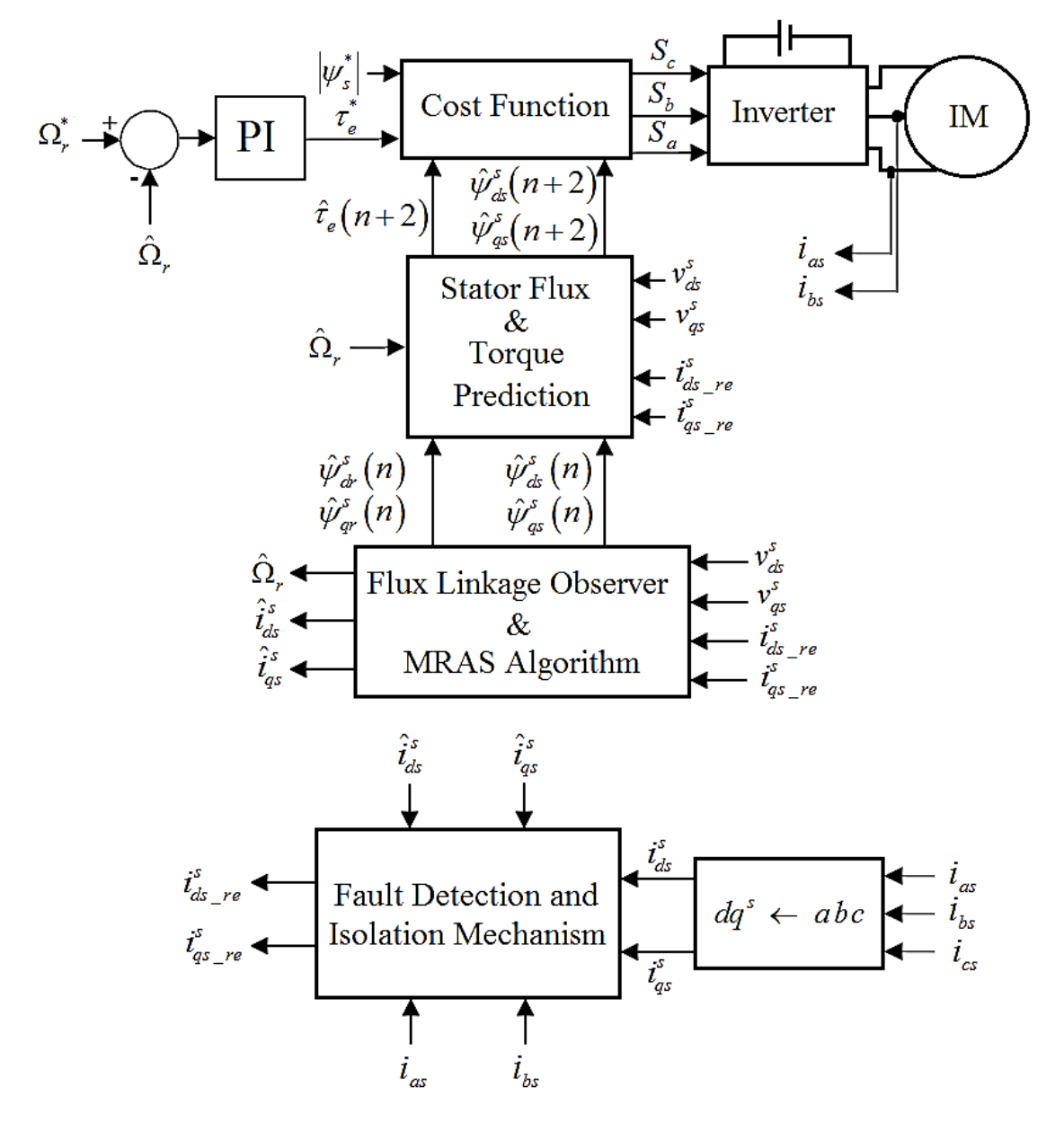


Figure 1: Proposed block diagram of the current sensor FTC method

The proposed current sensor FTC algorithm works based on a model predictive torque controlled three-phase IM using two current sensors. Two current sensors are placed in *a*-phase and *b*-phase. Based on this figure, a modified MPTC strategy, fault detection and isolation units, a MRAS estimator and flux linkage observer are combined. Initially, the fault detection and isolation units based on the TD algorithm and a logic circuit module recognize the CSF condition and select to use the actual stator currents or estimated stator currents. Based on the MRAS estimator, the three-phase motor speed is estimated. In addition, using the flux linkage observer the stator fluxes, rotor fluxes, and stator currents are calculated. It should be pointed out

that the reconstructed motor currents used in the MRAS estimator and flux linkage observer block are determined by the fault detection and isolation modules.

To compare the proposed scheme with the conventional MPTC, the schematic diagram of the conventional MPTC is given in Appendix A.

4. STRUCTURE OF THE USED ENCODERLESS MPTC STRATEGY FOR PRE-FAULT OPERATION

The used control strategy in this research is in accordance with a recently presented MPTC based method [9]. It is worth noting that in [9], a modified encoderless MPTC strategy using two EKFs was proposed for a healthy three-phase IM drive. However, the use of two EKFs considerably increases the control structure complexity and memory size needed for the real time implementation. The approach in [9] is suitably modified to make it appropriate for the current sensor FTC technique. The stator fluxes and electromagnetic torque at the instant (n+1) can be predicted as illustrated in (1)-(3):

$$\hat{\psi}_{ds}^{s}(n+1) = \hat{\psi}_{ds}^{s}(n) + v_{ds}^{s}(n)T_{s} - r_{s}i_{ds}^{s}(n)T_{s}$$
(1)

$$\hat{\psi}_{qs}^{s}(n+1) = \hat{\psi}_{qs}^{s}(n) + v_{qs}^{s}(n)T_{s} - r_{s}i_{qs}^{s}(n)T_{s}$$
(2)

$$\hat{\tau}_{e}(n+1) = \left(\frac{P}{2}\right) \left(i_{qs}^{s}(n+1)\hat{\psi}_{ds}^{s}(n+1) - i_{ds}^{s}(n+1)\hat{\psi}_{qs}^{s}(n+1)\right)$$
(3)

where,

$$i_{ds}^{s}(n+1) = i_{ds}^{s}(n) + \left(\frac{T_{s}}{L_{s} - \frac{L_{m}^{2}}{L_{r}}}\right) \left(v_{ds}^{s}(n) - r_{s}i_{ds}^{s}(n) + \left(\frac{L_{m}r_{r}}{L_{r}^{2}}\right) \left(\hat{\psi}_{dr}^{s}(n) - L_{m}i_{ds}^{s}(n)\right) + \left(\frac{L_{m}}{L_{r}}\right) \left(\hat{Q}_{r}\left(\frac{L_{m}}{L_{r}}\right) \left(\hat{\psi}_{qr}^{s}(n) - L_{m}i_{qs}^{s}(n)\right) + \left(\frac{L_{m}^{2}}{L_{r}}\right) \hat{Q}_{r}i_{qs}^{s}(n)\right)$$

$$(4)$$

$$i_{qs}^{s}(n+1) = i_{qs}^{s}(n) + \left(\frac{T_{s}}{L_{s} - \frac{L_{m}^{2}}{L_{r}}}\right) \left(v_{qs}^{s}(n) - r_{s}i_{qs}^{s}(n) + \left(\frac{L_{m}r_{r}}{L_{r}^{2}}\right) \left(\hat{\psi}_{qr}^{s}(n) - L_{m}i_{qs}^{s}(n)\right) + \left(\frac{L_{m}}{L_{r}}\right) \left(\hat{\Omega}_{r}\left(\frac{L_{m}}{L_{r}}\right) \left(\hat{\psi}_{dr}^{s}(n) - L_{m}i_{ds}^{s}(n)\right) + \left(\frac{L_{m}^{2}}{L_{r}}\right) \hat{\Omega}_{r}i_{ds}^{s}(n)\right)$$
(5)

From (1)-(5), it is observed that the stator fluxes and torque equations are affected by estimation errors of the fluxes and motor speed. In this study, the values of fluxes and

speed are estimated based on a flux linkage observer and MRAS algorithm as shown in the next section.

To compensate the time delay, the prediction of motor variables such as stator fluxes and electromagnetic torque is done at the instant (n+2) [31]. The stator fluxes and electromagnetic torque at the instant (n+2) can be predicted as demonstrated in (6)-(8):

$$\hat{\psi}_{ds}^{s}(n+2) = \hat{\psi}_{ds}^{s}(n+1) + v_{ds}^{s}(n+1)T_{s} - r_{s}i_{ds}^{s}(n+1)T_{s}$$
(6)

$$\hat{\psi}_{as}^{s}(n+2) = \hat{\psi}_{as}^{s}(n+1) + v_{as}^{s}(n+1)T_{s} - r_{s}i_{as}^{s}(n+1)T_{s}$$
(7)

$$\hat{\tau}_{e}(n+2) = \left(\frac{P}{2}\right) \left(i_{qs}^{s}(n+2)\hat{\psi}_{ds}^{s}(n+2) - i_{ds}^{s}(n+2)\hat{\psi}_{qs}^{s}(n+2)\right)$$
(8)

where,

$$\frac{i_{ds}^{s}(n+2) = i_{ds}^{s}(n+1) + \left(\frac{L_{m}r_{r}}{L_{s}}\right) \left(\hat{\psi}_{ds}^{s}(n+1) - r_{s}i_{ds}^{s}(n+1) + \left(\frac{L_{m}r_{r}}{L_{r}^{2}}\right) \left(\hat{\psi}_{dr}^{s}(n+1) - L_{m}i_{ds}^{s}(n+1)\right) + \left(\frac{L_{m}}{L_{r}}\right) \left(\hat{\psi}_{qr}^{s}(n+1) - L_{m}i_{qs}^{s}(n+1)\right) + \left(\frac{L_{m}^{2}}{L_{r}}\right) \hat{\Omega}_{r}i_{qs}^{s}(n+1) \right)$$
(9)

$$\frac{i_{qs}^{s}(n+2) = i_{qs}^{s}(n+1) + \left(\frac{L_{m}r_{r}}{L_{s}}\right) \left(\hat{\psi}_{qr}^{s}(n+1) - L_{m}i_{qs}^{s}(n+1) + \left(\frac{L_{m}r_{r}}{L_{r}^{2}}\right) \left(\hat{\psi}_{qr}^{s}(n+1) - L_{m}i_{qs}^{s}(n+1)\right) + \hat{\Omega}_{r}\left(\frac{L_{m}}{L_{r}}\right) \left(\hat{\psi}_{dr}^{s}(n+1) - L_{m}i_{ds}^{s}(n+1)\right) + \left(\frac{L_{m}^{2}}{L_{r}}\right) \hat{\Omega}_{r}i_{ds}^{s}(n+1) \right)$$
(10)

Since the frequency of the rotor flux is too low compared with the sampling frequency, in (9) and (10) it is assumed that $\hat{\psi}_r^s(n+1) = \hat{\psi}_r^s(n)$ [9]. In addition, $i_{ds}^s(n+1)$ and $i_{qs}^s(n+1)$ in (9) and (10) are obtained based on (4) and (5).

As a result, according to (1)-(10), the stator fluxes and electromagnetic torque at the instant (n+2) can be predicted as (11)-(13):

$$\hat{\psi}_{ds}^{s}(n+2) = \hat{\psi}_{ds}^{s}(n) + v_{ds}^{s}(n)T_{s} - r_{s}i_{ds}^{s}(n)T_{s} + v_{ds}^{s}(n+1)T_{s} - \left[i_{ds}^{s}(n) + \left(\frac{T_{s}}{L_{s}} \right) \left(v_{ds}^{s}(n) - r_{s}i_{ds}^{s}(n) + \left(\frac{L_{m}r_{r}}{L_{r}^{2}} \right) \left(\hat{\psi}_{dr}^{s}(n) - L_{m}i_{ds}^{s}(n) \right) + \left(\frac{T_{s}}{L_{r}} \right) \hat{\Omega}_{r}i_{qs}^{s}(n) \right] \right] T_{s}$$

$$(11)$$

$$\hat{\psi}_{qs}^{s}(n+2) = \hat{\psi}_{qs}^{s}(n) + v_{qs}^{s}(n)T_{s} - r_{s}i_{qs}^{s}(n)T_{s} + v_{qs}^{s}(n+1)T_{s} - \left[i_{qs}^{s}(n) + \left(\frac{T_{s}}{L_{s}} \right) \left(v_{qs}^{s}(n) - r_{s}i_{qs}^{s}(n) + \left(\frac{L_{m}r_{r}}{L_{r}} \right) \left(\hat{\psi}_{qr}^{s}(n) - L_{m}i_{qs}^{s}(n) \right) + \left(\frac{T_{s}}{L_{s}} \right) \left(\hat{\Omega}_{r} \left(\frac{L_{m}}{L_{r}} \right) \left(\hat{\psi}_{dr}^{s}(n) - L_{m}i_{ds}^{s}(n) \right) + \left(\frac{L_{m}^{2}}{L_{r}} \right) \hat{\Omega}_{r}i_{ds}^{s}(n) \right) \right] T_{s}$$

$$(12)$$

$$\hat{\tau}_{e}(n+2) = \left(\frac{P}{2}\right) \left(i_{qs}^{s}(n+2)\hat{\psi}_{ds}^{s}(n+2) - i_{ds}^{s}(n+2)\hat{\psi}_{qs}^{s}(n+2)\right)$$
(13)

In (13), $\hat{\psi}_{ds}^s(n+2)$ and $\hat{\psi}_{qs}^s(n+2)$ are calculated based on (11) and (12). In addition, $i_{ds}^s(n+2)$ and $i_{qs}^s(n+2)$ in (13) are obtained based on (4), (5), (9), and (10).

As a result, $\hat{\psi}_{ds}^{s}(n+2)$, $\hat{\psi}_{qs}^{s}(n+2)$ and $\hat{\tau}_{e}(n+2)$ are predicted by discrete prediction equations (11)-(13).

To achieve the optimal voltage vectors for inverter feeding, the following cost function is considered:

$$F = \left| \tau_e^* (n+2) - \hat{\tau}_e (n+2) \right| + \lambda_{\psi} \left\| \psi_s^* \right| - \left| \hat{\psi}_s (n+2) \right| + i_m$$
 (14)

where [9],

$$i_{m} = \begin{cases} \infty & \text{if } \left| i_{s} \left(n+2 \right) \right| > i_{\text{max}} \\ 0 & \text{otherwise} \end{cases}$$
 (15)

As can be seen from (14), the term i_m is added to the cost function to protect over current.

Based on (1)-(15), Figure 2 is presented for encoderless MPTC of three-phase IMs.

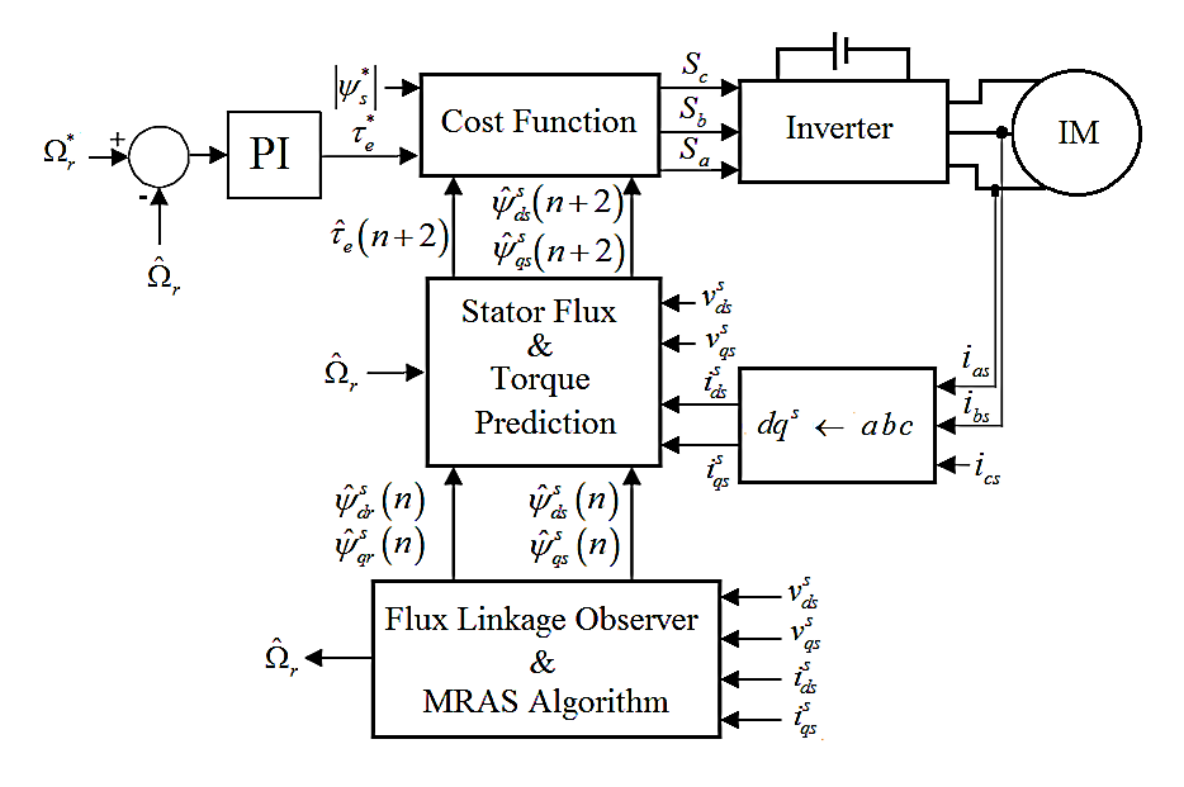


Figure 2: Encoderless MPTC of three-phase IMs

In Figure 2, the estimated speed is compared with the desired speed to produce the desired electromagnetic torque. According to the stator voltages, stator currents, and estimated values of the fluxes and speed, the stator fluxes and electromagnetic torque are predicted at the instant (n+2). Finally, the optimal voltage vectors for inverter feeding are achieved based on the cost function.

5. ESTIMATION MECHANISMS FOR THE ROTOR SPEED, STATOR CURRENTS, AND FLUXES BASED ON MRAS AND FLUX LINKAGE OBSERVER

As can be realized from Figure 2, the values of fluxes and speed are required in the control system. In this paper, a MRAS and flux linkage observer module is used for estimation of the rotor speed, stator currents, and fluxes.

5.1 Rotor speed estimation using MRAS

MRAS algorithm has been proved to be an efficient and straightforward approach for encoderless control of three-phase IM drives [7]. The speed estimation technique in this study is based on the conventional MRAS based on the rotor flux. The structure of the conventional MRAS for speed estimation is illustrated in Figure 3.

As shown in Figure 3, the rotor fluxes in the reference model $(\psi_{dr1}^s, \psi_{qr1}^s)$ are computed using the voltages and currents. Moreover, the rotor fluxes in the adjustable model $(\psi_{dr2}^s, \psi_{qr2}^s)$ are computed according to the currents and estimated speed. The error between the reference model quantities and adjustable model quantities is fed to the adaptation mechanism to produce the rotor speed. It can be mentioned that the proposed encoderless FTC system can work for all speed estimation strategies. Here, MRAS is used only as a sample.

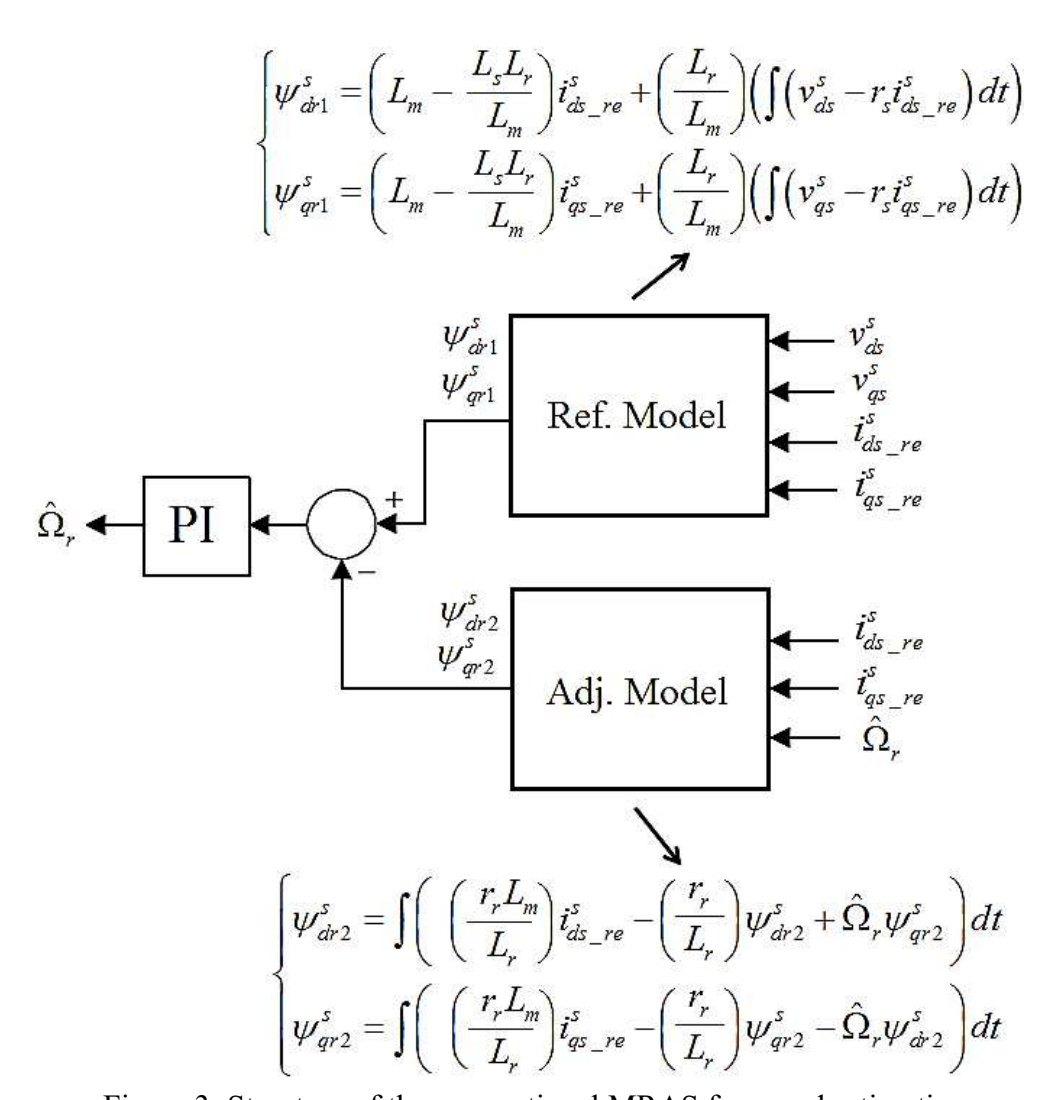


Figure 3: Structure of the conventional MRAS for speed estimation

5.2 Stator currents and fluxes estimation based on a flux linkage observer

In the rotational reference frame, the motor dq fluxes $(\hat{\psi}_{dm}^e, \hat{\psi}_{qm}^e, \hat{\psi}_{ds}^e, \hat{\psi}_{qs}^e, \hat{\psi}_{dr}^e, \hat{\psi}_{qr}^e)$, $\hat{\Omega}_{sl}$, and $\hat{\theta}_e$ can be shown as (16)-(23):

$$\hat{\psi}_{dm}^{e} = \left(\frac{L_{m1}}{L_{ls}}\right) \hat{\psi}_{ds}^{e} + \left(\frac{L_{m1}}{L_{lr}}\right) \hat{\psi}_{dr}^{e} \tag{16}$$

$$\hat{\psi}_{qm}^{e} = \left(\frac{L_{m1}}{L_{ls}}\right) \hat{\psi}_{qs}^{e} + \left(\frac{L_{m1}}{L_{lr}}\right) \hat{\psi}_{qr}^{e} \tag{17}$$

$$\hat{\psi}_{ds}^{e} = \int \left(v_{ds}^{e} + \hat{\Omega}_{e} \hat{\psi}_{qs}^{e} - \left(\frac{r_{s}}{L_{ls}} \right) \left(\hat{\psi}_{ds}^{e} - \hat{\psi}_{dm}^{e} \right) \right) dt \tag{18}$$

$$\hat{\psi}_{qs}^{e} = \int \left(v_{qs}^{e} - \hat{\Omega}_{e} \hat{\psi}_{ds}^{e} - \left(\frac{r_{s}}{L_{ls}} \right) \left(\hat{\psi}_{qs}^{e} - \hat{\psi}_{qm}^{e} \right) \right) dt \tag{19}$$

$$\hat{\psi}_{dr}^{e} = \int \left(\left(\hat{\Omega}_{e} - \hat{\Omega}_{r} \right) \hat{\psi}_{qr}^{e} - \left(\frac{r_{r}}{L_{lr}} \right) \left(\hat{\psi}_{dr}^{e} - \hat{\psi}_{dm}^{e} \right) \right) dt \tag{20}$$

$$\hat{\psi}_{qr}^{e} = \int \left(-\left(\hat{\Omega}_{e} - \hat{\Omega}_{r}\right) \hat{\psi}_{dr}^{e} - \left(\frac{r_{r}}{L_{lr}}\right) \left(\hat{\psi}_{qr}^{e} - \hat{\psi}_{qm}^{e}\right) \right) dt \tag{21}$$

$$\hat{\Omega}_{sl} = \hat{\Omega}_{e} - \hat{\Omega}_{r} = \frac{0.5 \left(\hat{\psi}_{ds}^{e} \hat{i}_{qs}^{e} r_{r} - \hat{\psi}_{qs}^{e} \hat{i}_{ds}^{e} r_{r} \right)}{\hat{\psi}_{dm}^{e} + \hat{\psi}_{qm}^{e}}$$
(22)

$$\hat{\theta}_e = \int \hat{\Omega}_e dt \tag{23}$$

where,

$$L_{m1} = \frac{L_m L_{ls} L_{lr}}{L_{ls} L_{lr} + L_m L_{lr} + L_m L_{ls}}$$
 (24)

In addition, the dq currents in terms of motor fluxes can be written as [32]:

$$\hat{i}_{ds}^{e} = \frac{\hat{\psi}_{ds}^{e} - \hat{\psi}_{dm}^{e}}{L_{t_{c}}} \tag{25}$$

$$\hat{i}_{qs}^{e} = \frac{\hat{\psi}_{qs}^{e} - \hat{\psi}_{qm}^{e}}{L_{ls}}$$
 (26)

Based on (16)-(26), the flux linkage observer module for estimation of the stator currents and fluxes is shown in Figure 4.

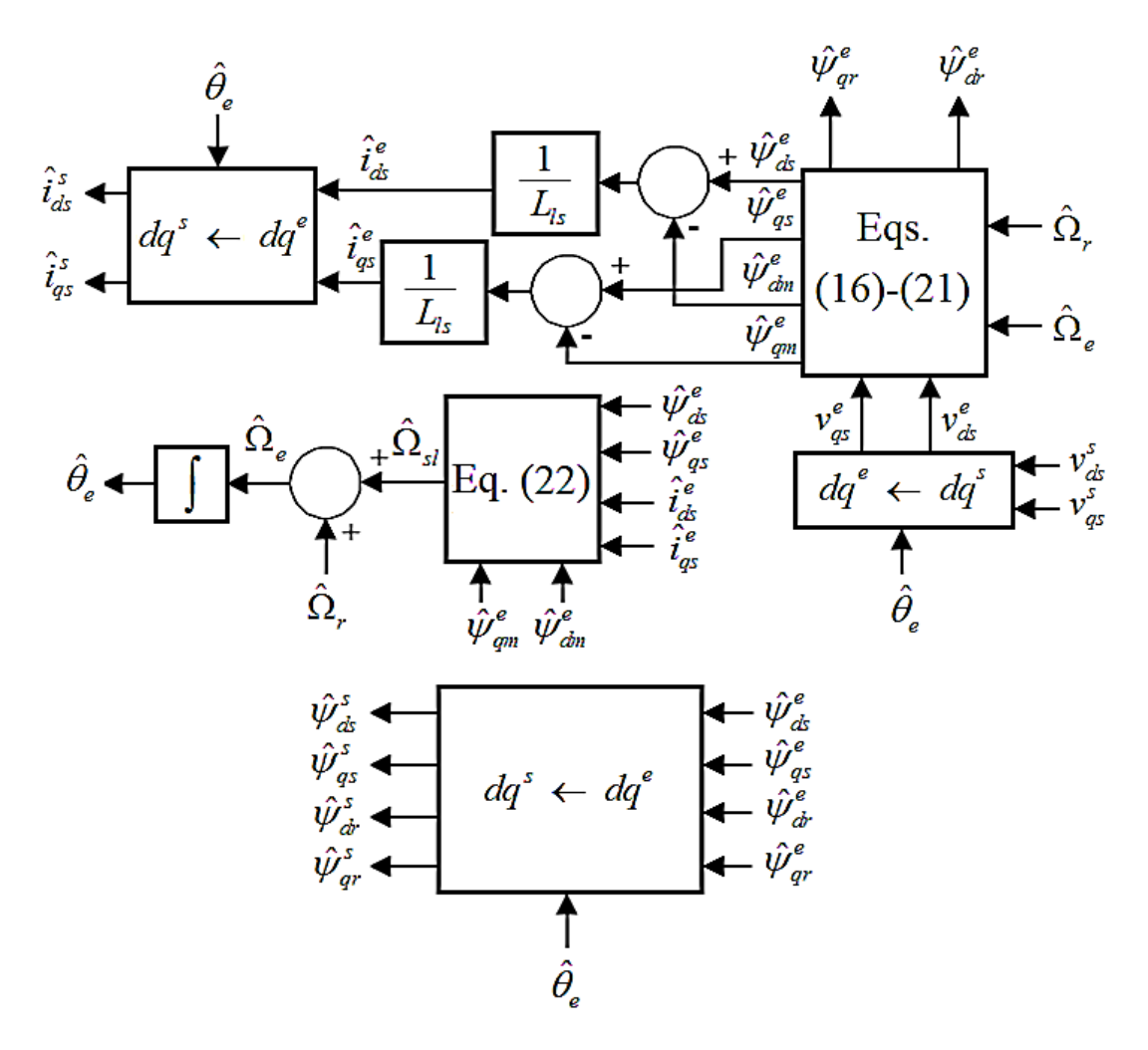


Figure 4: Flux linkage observer module

In Figure 4, $dq^s \rightarrow dq^e$ is:

$$T(\theta_e) = \begin{bmatrix} \cos \theta_e & \sin \theta_e \\ -\sin \theta_e & \cos \theta_e \end{bmatrix}$$
 (27)

6. CSF DETECTION AND ISOLATION METHODS

6.1 Fault detection

In the proposed encoderless FTC algorithm, the fault detection is done by TD of the three-phase IM line currents. This method is able to detect even a slight change in the motor currents [33]. In this research, two TDs are utilized in phases a and b to detect the fault. The TDs can be determined using some simple calculations as (28) and (29):

$$\Delta^3 i_s = \Delta^2 i_{s1} - \Delta^2 i_{s0} \tag{28}$$

where,

$$\Delta^{2} i_{s0} = \Delta i_{s1} - \Delta i_{s0} , \qquad \Delta^{2} i_{s1} = \Delta i_{s2} - \Delta i_{s1}
\Delta i_{s0} = i_{s1} - i_{s0} , \qquad \Delta i_{s1} = i_{s2} - i_{s1} , \qquad \Delta i_{s2} = i_{s3} - i_{s2}$$
(29)

Under healthy and faulty conditions, the TD related to any line current generates very small and high impulse amplitudes, respectively. The fault detection is based on the comparison between the absolute value of the TD and a predefined threshold (T), as shown in Table 1.

Measurements	Calculations	Comparisons	Conditions
	TD_a	if $(TD_a \ge T)$	Faulty condition
i_{as} and i_{bs}	and	if $\left(TD_a < T \& TD_b < T \right)$	Normal condition
	TD_b	if $(TD_a < T \& TD_b \ge T)$	Faulty condition

Table 1: CSF detection system

The selection of an appropriate value for threshold is a cumbersome task. Nevertheless, to obtain the value of *T*, some simulations based on Figure 2 during different operating conditions were carried out. The parameters and nominal values of the 4-pole, 50 Hz, 0.75 kW wye-connected three-phase IM drive as well as the controller and inverter parameters in simulations are given in Appendix B.

Tables 2-6 show the absolute values of TD_a and TD_b at the CSF occurrence during different operating conditions.

Table 2: Absolute values of TD_a and TD_b when $\Omega_r^* = 10 \text{ rad/s}$

		$\theta_e = 0^{\circ}$	$\theta_e = 90^{\circ}$	$\theta_e = 175^{\circ}$	$\theta_e = 225^{\circ}$	$\theta_e = 315^{\circ}$	$\theta_e = 350^{\circ}$
TD	τ _l =0 N.m	1.6 A	1.8 A	2.4 A	5.6 A	16.1 A	10.5 A
TD_a	τ _l =0.5 N.m	1.4 A	2 A	3.1 A	4.4 A	12.1 A	9.2 A
TD_b	τ _l =0 N.m	2.6 A	1.3 A	3 A	4.1 A	9.1 A	7.7 A
D_b	τ _l =0.5 N.m	1.2 A	2.2 A	3.7 A	5.1 A	14.1 A	11 A

Table 3: Absolute values of TD_a and TD_b when $\Omega_r^* = 40 \text{ rad/s}$

		$\theta_e = 0^{\circ}$	$\theta_e = 90^{\circ}$	$\theta_e = 175^{\circ}$	$\theta_e = 225^{\circ}$	$\theta_e = 315^{\circ}$	$\theta_e = 350^{\circ}$
TD	$\tau_l=0 \text{ N.m}$	1.05 A	2.4 A	4.4 A	16.6 A	10.3 A	9.5 A
TD_a	τ _l =1 N.m	1.1 A	3.1 A	4.1 A	15.4 A	15.1 A	14.2 A
TD	τ _l =0 N.m	1.3 A	1.9 A	4.1 A	16.3 A	9.1 A	8.5 A
TD_b	τ _l =1 N.m	1.4 A	3.4 A	4.2 A	14.4 A	13.1 A	12.2 A

Table 4: Absolute values of TD_a and TD_b when $\Omega_r^* = 90 \text{ rad/s}$

		$\theta_e = 0^{\circ}$	$\theta_e = 90^{\circ}$	$\theta_e = 175^{\circ}$	$\theta_e = 225^{\circ}$	$\theta_e = 315^{\circ}$	$\theta_e = 350^{\circ}$
TD	τ _l =1 N.m	5.6 A	10.8 A	12.3 A	11.6 A	10.3 A	7.5 A
TD_a	$\tau_l=2 \text{ N.m}$	7.4 A	10.7 A	16.02 A	15.4 A	15.1 A	13.3 A
TD	$\tau_l=1 \text{ N.m}$	3.3 A	6.7 A	12.7 A	10.6 A	8.7 A	6.5 A
TD_b	τ _l =2 N.m	1.8 A	4.3 A	14.4 A	13.9 A	12.5 A	9.9 A

Table 5: Absolute values of TD_a and TD_b when $\Omega_r^* = 120 \text{ rad/s}$

		$\theta_e = 0^{\circ}$	$\theta_e = 90^{\circ}$	$\theta_e = 175^{\circ}$	$\theta_e = 225^{\circ}$	$\theta_e = 315^{\circ}$	$\theta_e = 350^{\circ}$
TD	τ _l =3 N.m	1.02 A	3.8 A	8.8 A	16.5 A	14.1 A	13.1 A
TD_a	$\tau_l=4 \text{ N.m}$	1.3 A	4 A	7.2 A	16.4 A	15.3 A	13.7 A
TD	τ _l =3 N.m	1.05 A	1.8 A	6.4 A	14 A	13.1 A	12.7 A
TD_b	τ _l =4 N.m	1.7 A	2 A	4.1 A	15.3 A	15.1 A	13.3 A

Table 6: Absolute values of TD_a and TD_b when $\Omega_r^* = 150 \text{ rad/s}$

		$\theta_e = 0^{\circ}$	$\theta_e = 90^{\circ}$	$\theta_e = 175^{\circ}$	$\theta_e = 225^{\circ}$	$\theta_e = 315^{\circ}$	$\theta_e = 350^{\circ}$
TD	$\tau_l=0 \text{ N.m}$	1.4 A	5.8 A	16.4 A	15.6 A	10.2 A	9.7 A
TD_a	τ _l =5.1 N.m	1.2 A	4.4 A	13.2 A	10.4 A	7.7 A	6.9 A
TD_b	τ _l =0 N.m	2.7 A	5.8 A	14.1 A	12.6 A	11.1 A	9.9 A
$ D_b $	τ _l =5.1 N.m	3.4 A	7.4 A	11.9 A	10.1 A	8.1 A	7.5 A

As shown in Tables 2-6, the absolute values of TD_a and TD_b at the CSF occurrence produce high impulse amplitude (in the range of 1.02 A to 16.6 A). It

should be pointed out that under normal state, the absolute values of TD_a and TD_b produce very small impulse amplitude (less than 0.01 A). These tables show that T =0.6 A, gives an acceptable performance of the proposed FTC method for all the fault condition.

6.2 Fault isolation

The dq currents in the stationary reference frame (superscript "s") and during healthy condition can be shown as (30):

$$\begin{bmatrix} i_{ds}^{s} \\ i_{qs}^{s} \end{bmatrix} = \sqrt{\frac{2}{3}} \begin{bmatrix} 1 & -\frac{1}{2} & -\frac{1}{2} \\ 0 & \frac{\sqrt{3}}{2} & -\frac{\sqrt{3}}{2} \end{bmatrix} \begin{bmatrix} i_{as} \\ i_{bs} \\ i_{cs} \end{bmatrix}$$
(30)

According to (30), i_{ds}^{s} and i_{qs}^{s} can be re-written as:

$$i_{ds}^{s} = \sqrt{\frac{3}{2}}i_{as} \tag{31}$$

$$i_{qs}^{s} = \sqrt{\frac{2}{3}} \left(\frac{\sqrt{3}}{2} i_{as} + \sqrt{3} i_{bs} \right)$$
 (32)

It is seen that the stator d-axis current only depends on the stator a-phase current, while the stator q-axis current depends on the stator a-phase and b-phase currents. It means that when the fault occurs in phase a, \hat{i}_{ds}^s and \hat{i}_{qs}^s (estimated values of the stator dq currents) should be utilized in the control system. Furthermore, when the CSF occurs in phase b, i_{ds}^s and \hat{i}_{qs}^s should be utilized in the control system. Additionally, during healthy mode, i_{ds}^s and i_{qs}^s should be used. Based on the above discussion, the fault detection and isolation scheme are shown in Figure 5.

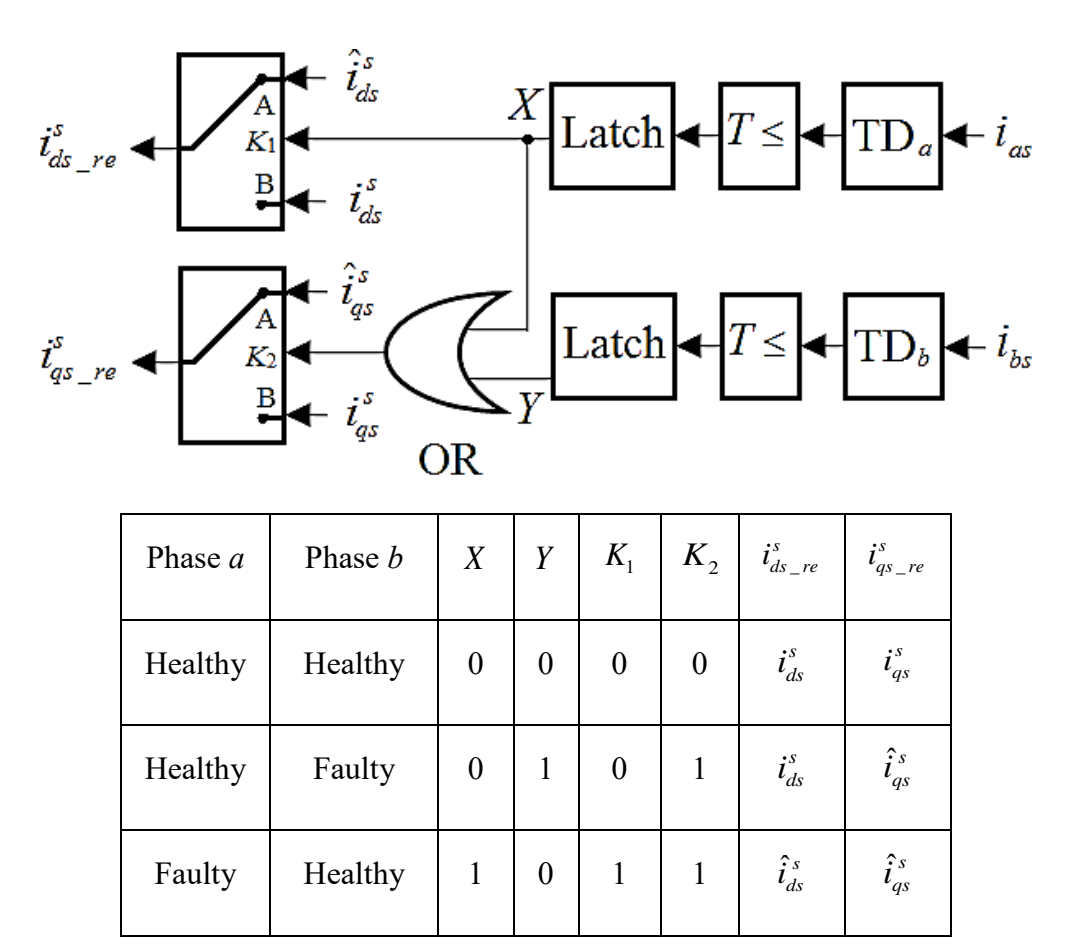


Figure 5: Fault detection and isolation scheme

As can be seen from the schematic diagram of Figure 5, after the fault detection process using TD operator, for continuous operation of the drive system, the logic circuit module selects the appropriate value of motor dq currents based on the X and Y values.

When X=0 and Y=0, it indicates that the sensors are healthy, and the dq currents are obtained from the actual dq currents.

When X=0 and Y=1, it means that the b-phase CSF happens. In this condition, the d-axis current is obtained from the actual d-axis current and the q-axis current is obtained from the estimated q-axis current.

When X=1 and Y=0, it can be concluded that the a-phase CSF happens. In this case, the dq currents are obtained from the estimated dq currents.

In summary, Figure 6 illustrates the detailed flowchart for the faulty sensor identification and suitable selection of the motor currents.

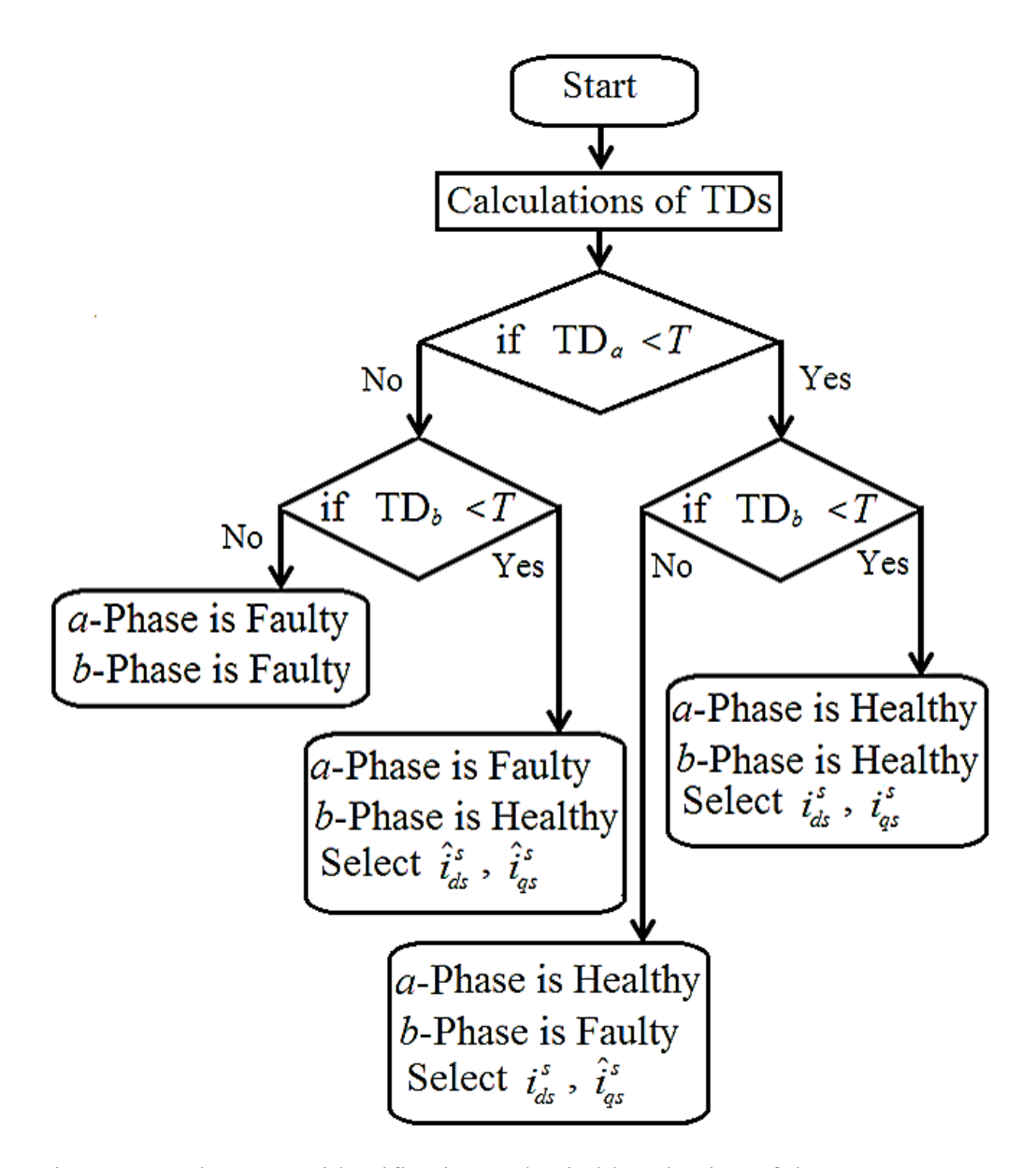


Figure 6: Faulty sensor identification and suitable selection of the motor currents

7. EXPERIMENTAL EVALUATION

The usefulness of the proposed FTC system for a MPTC-based three-phase IM drive is confirmed with a TMS320F28335 controller board from a prototype developed in the lab. The picture of the experimental setup of a 0.75 kW wye-connected three-phase IM drive using the proposed FTC algorithm is displayed in Figure 7.

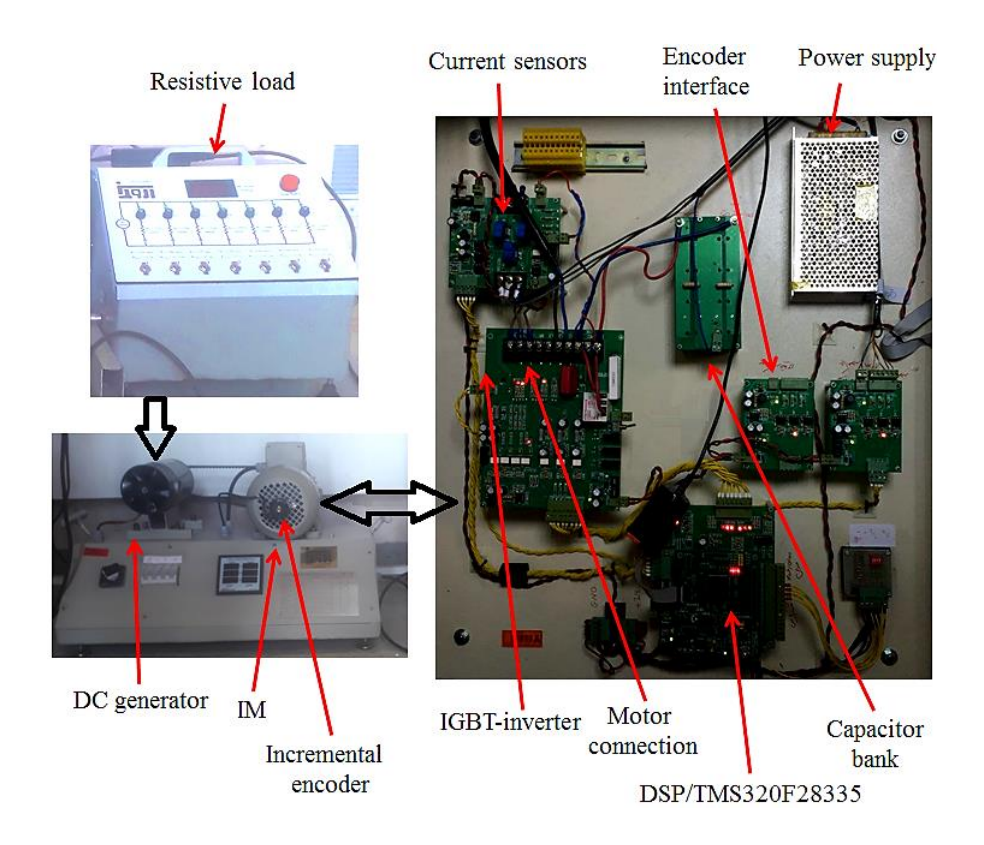


Figure 7: Picture of the experimental setup

The proposed FTC technique code for the TMS320F28335 controller board is generated using PSIM software. In all tests, the electromagnetic torque is calculated based on the IM equations. The parameters and nominal values of the experimented three-phase IM as well as the controller and inverter parameters are given in Appendix B. In tests, the sensor output is made zero in the software. It should be pointed out that the sensor faults do not essentially mean an open-circuit fault; any malfunctions in current sensors can be considered as the sensor fault in the present study.

In many industrial applications such as railway traction, electric vehicles, etc. the drive system should be able to control the IM for the entire speed range [34-36]. For this aim, different operating conditions such as high speed (Figure 11, Figure 13, and Figure 14), medium speed (Figure 8, Figure 10, and Figure 12), and low speed (Figure 9) are considered in tests.

Additionally, in many industries the drive system should be able to control the machine during light or mid load conditions such as small fan and electric vehicle applications and heavy load conditions such as electric traction and cooling pumps [37,38]. In tests, Figure 9 and Figure 13 are presented to evaluate the control system performance during light or mid load conditions, while Figure 11 is presented to evaluate the control system performance during the heavy load condition.

7.1 Performance of the proposed FTC strategy when *a*-phase and *b*-phase sensors are healthy

Figure 8 displays the results of the suggested FTC scheme under the condition mentioned above. In Figure 8, the reference speed is changed from 110 rad/s to 70 rad/s, $\tau_l=0$ N.m and $|\psi_s^*|=1$ Wb.

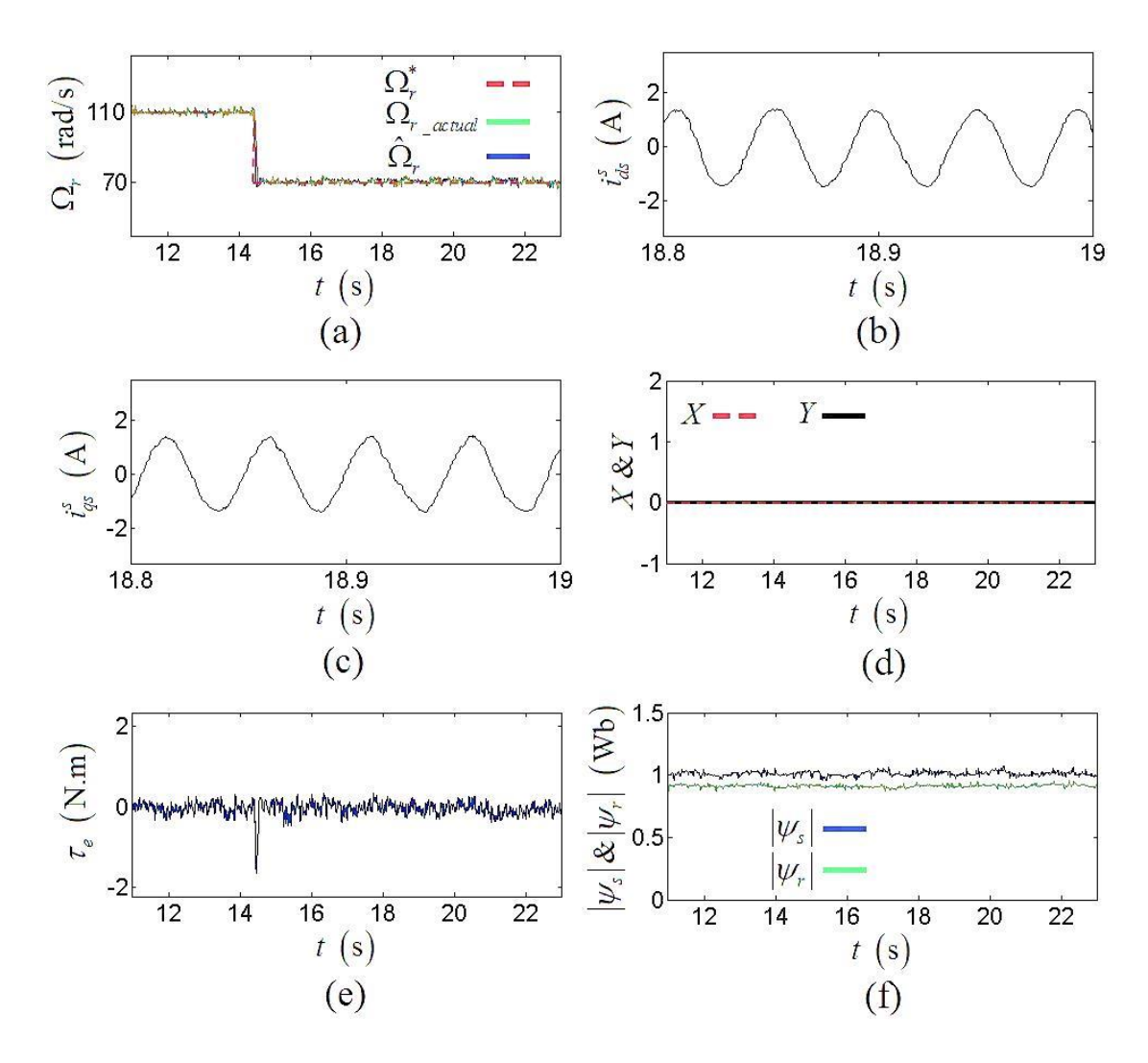


Figure 8: Performance of the proposed FTC strategy during no-load condition when a-phase and b-phase sensors are healthy; (a) $\Omega_r^*, \hat{\Omega}_r, \Omega_{r_actual}$, (b) i_{ds}^s , (c) i_{qs}^s , (d) X & Y, (e) τ_s , (f) $|\psi_s| \& |\psi_r|$

It is seen that the actual and estimated speeds follow the reference speed. As shown in Figure 8(f), the amplitudes of the estimated fluxes have constant values and the estimated stator flux amplitude tracks the command stator flux. As can be seen from Figures 8(b) and 8(c), the actual dq currents are sinusoidal and balanced in this

condition. As shown in Figure 8(d), the values of X and Y are 0 and 0, respectively. Thus, i_{ds}^s and i_{qs}^s are selected as feedback currents. Figure 8(e) shows the torque performance during healthy condition. In his test, the average value of the torque during the steady-state and no-load condition is around 0.25 N.m.

Figure 9 demonstrates the experimental results of the proposed FTC strategy during normal condition and different speeds. In this test, the reference speed is changed from 5 rad/s to 17 rad/s to 75 rad/s, τ_l is changed from 0 N.m to 2 N.m (no-load condition to 39 % of the nominal load) at t=70.5 s, and $|\psi_s^*|=1$ Wb.

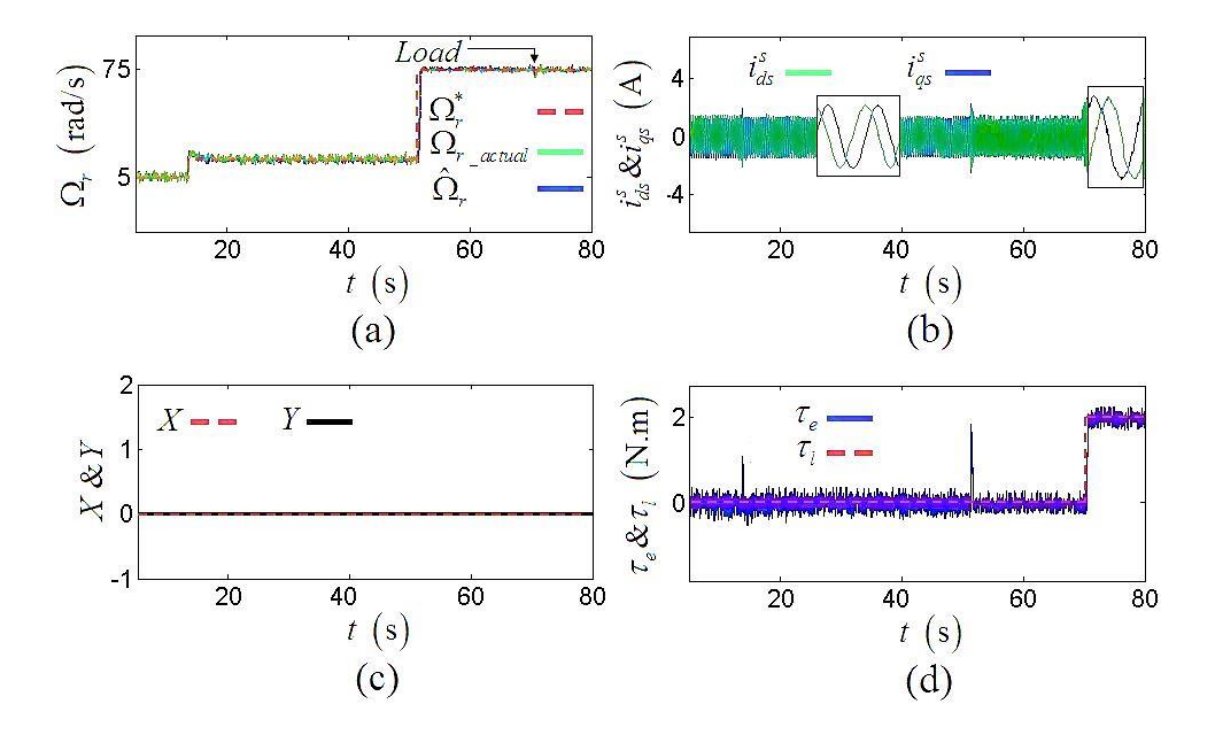


Figure 9: Performance of the proposed FTC strategy during load condition when a-phase and b-phase sensors are healthy; (a) $\Omega_r^*, \hat{\Omega}_r, \Omega_{r_actual}$, (b) $i_{ds}^s \& i_{qs}^s$, (c) X & Y, (d) $\tau_e \& \tau_l$

It is observed that the actual and estimated speeds track the command speed during low and high speeds. Furthermore, in this condition, the dq currents are sinusoidal and balanced. Additionally, the values of X and Y are both 0. Finally, the average value of torque is equal to the applied mechanical load. In this test, the average value of the torque during the steady-state and after the load is around 0.33 N.m which is similar to the average value of the torque in Figure 9.

The achieved results in Figure 9 clearly show the excellent performance of the introduced FTC strategy during normal mode and under different speeds and load condition.

7.2 Performance of the proposed FTC strategy when *a*-phase sensor is faulty and *b*-phase sensor is healthy

Figure 10 shows the performance of the suggested FTC algorithm when the sensor fault happens in phase a while the sensor in phase b is healthy. In this experiment, the drive system was initially working with healthy sensors and at t=14 s, the a-phase sensor output is made zero using a simple switching block in PSIM. In this test, the reference speed is 70 rad/s, τ_l =0 N.m, and $|\psi_s^*|$ =1 Wb.

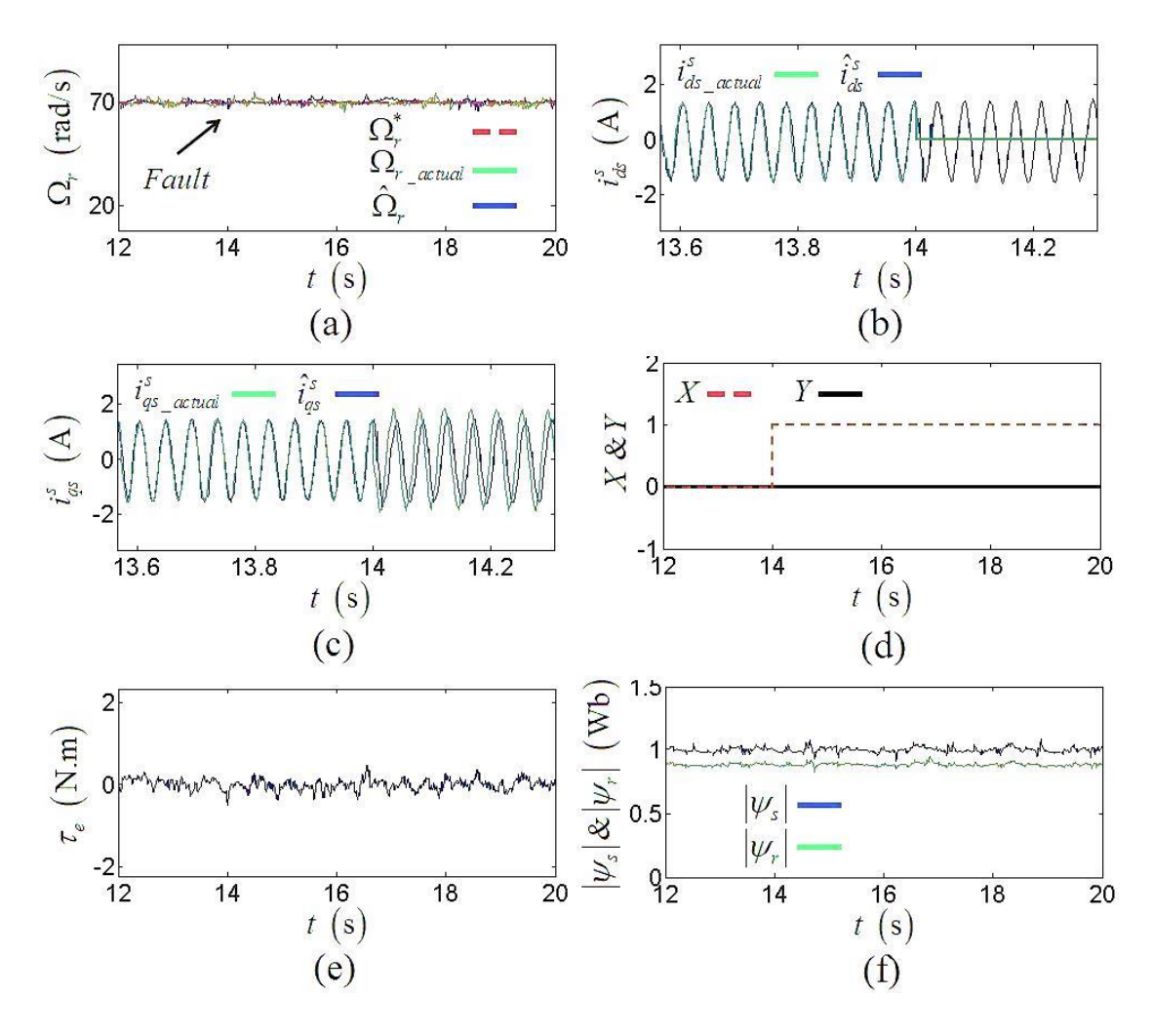


Figure 10: Performance of the proposed FTC strategy during no-load condition when a-phase sensor is faulty and b-phase sensor is healthy; (a) $\Omega_r^*, \hat{\Omega}_r, \Omega_{r_actual}$, (b) i_{ds}^s , (c)

$$i_{qs}^{s}$$
 , (d) $X \& Y$, (e) τ_{e} , (f) $|\psi_{s}| \& |\psi_{r}|$

Figure 10(a) and Figure 10(f) show undisturbed estimated speed, actual speed, and estimated fluxes during the post-fault operation. The amplitudes of the estimated stator and rotor fluxes in Figure 10(f) depict the constant operations of the fluxes even during a-phase current sensor failure. As discussed before, when the CSF happens in phase a, actual dq currents have incorrect values (see Figure 10(b) and Figure 10(c)). As can be seen from Figure 10(d), after the sensor fault, the values of X and Y are 1 and 0, respectively. Thus, \hat{i}_{ds}^s and \hat{i}_{qs}^s are selected as feedback signals. Figure 10(e) demonstrates acceptable ripples of the torque signal during post-fault operation as the average value of the torque before the CSF is around 0.23 N.m and the average value of the torque after the CSF is around 0.32 N.m. Figure 10 shows that the proposed system can suitably detect the fault and swaps from the actual motor currents to the estimated motor currents under such a situation.

Figure 11 displays the performance of the proposed method during load condition. As shown in Figure 11, in this test the drive system starts with healthy sensors and under no-load condition. Then, a mechanical load equal to 5.1 N.m (nominal load) is applied. Afterward, *a*-phase CSF happens. In Figure 11, the reference speed is 150 rad/s and $|\psi_s^*|=1$ Wb.

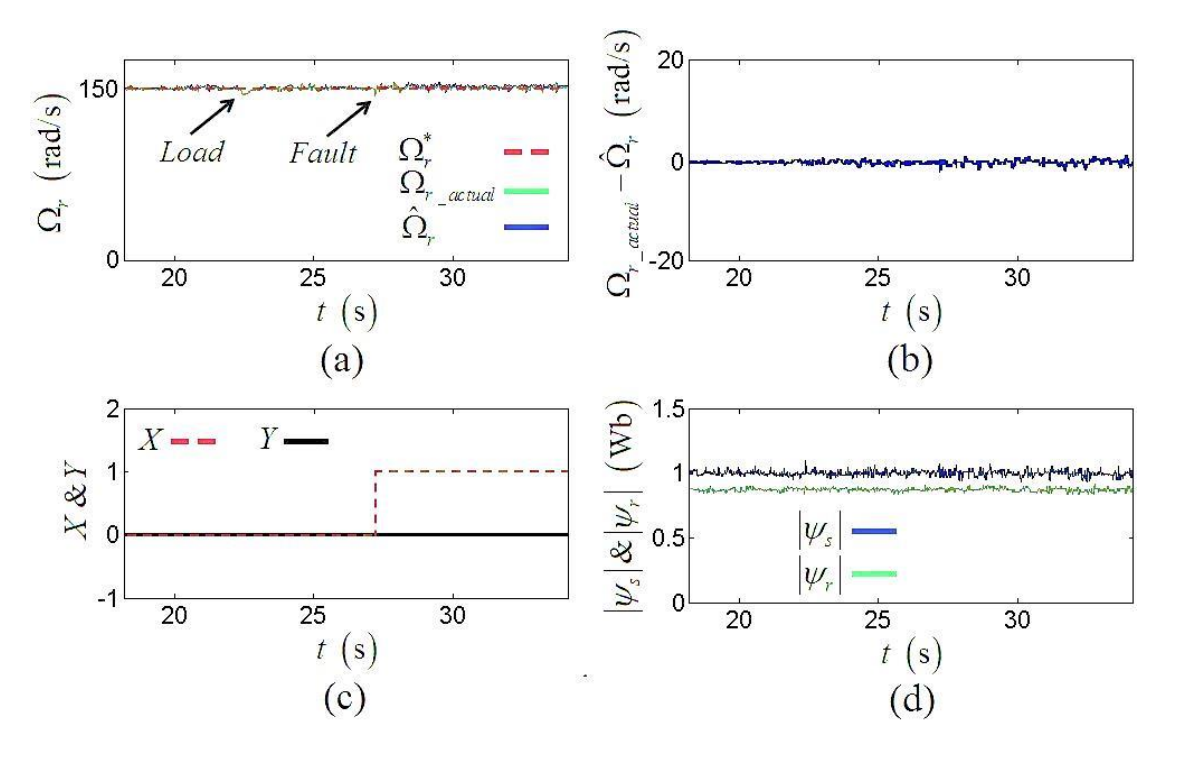


Figure 11: Performance of the proposed FTC strategy during load condition when a-phase sensor is faulty and b-phase sensor is healthy; (a) $\Omega_r^*, \hat{\Omega}_r, \Omega_r$ actual, (b)

$$\Omega_{r \ actual} - \hat{\Omega}_{r}$$
, (c) $X \& Y$, (d) $|\psi_{s}| \& |\psi_{r}|$

Figure 11(a) shows that the estimated and actual speeds can track the command speed. The speed error is presented in Figure 11(b). Based on Figure 11(b), the average value of the speed error is near zero. As shown in Figure 11(c), i_{ds}^s and i_{qs}^s are used during normal mode. In addition, \hat{i}_{ds}^s and \hat{i}_{qs}^s are used during the faulty mode. As shown in Figure 11(d), the amplitudes of the fluxes have constant values and the stator flux amplitude follows the command stator flux.

7.3 Performance of the proposed FTC strategy when a-phase sensor is healthy and b-phase sensor is faulty

The performance of the proposed FTC algorithm under such a situation is illustrated in Figure 12. In this scenario, during pre-fault operation, the reference speed is 90 rad/s and after the CSF, the reference speed is changed from 90 rad/s to 120 rad/s, $\tau_l=0$ N.m, and $|\psi_s^*|=1$ Wb.

Figure 12(a) and Figure 12(f) show the actual speed, estimated speed, and estimated fluxes have uninterrupted and continuous tracking performances in the presence of b-phase sensor fault. Figure 12(f) also shows the constant values of fluxes during different modes and speeds. As shown in this scenario and during post-fault operation i_{ds}^s has a correct value while the value of i_{qs}^s has a wrong value (see Figure 12(b) and Figure 12(c)). As can be observed from Figure 12(d), in this condition, the values of X and Y are 0 and 1, respectively. It means that i_{ds}^s and i_{qs}^s are used in the control system. Figure 12(e) shows the torque signal has low ripples during different conditions and its variation is proportional to the motor speed. In this test, the average value of the torque during the steady-state and after the CSF is around 0.34 N.m while the average value of the torque during the steady-state and before the CSF is around 0.25 N.m.

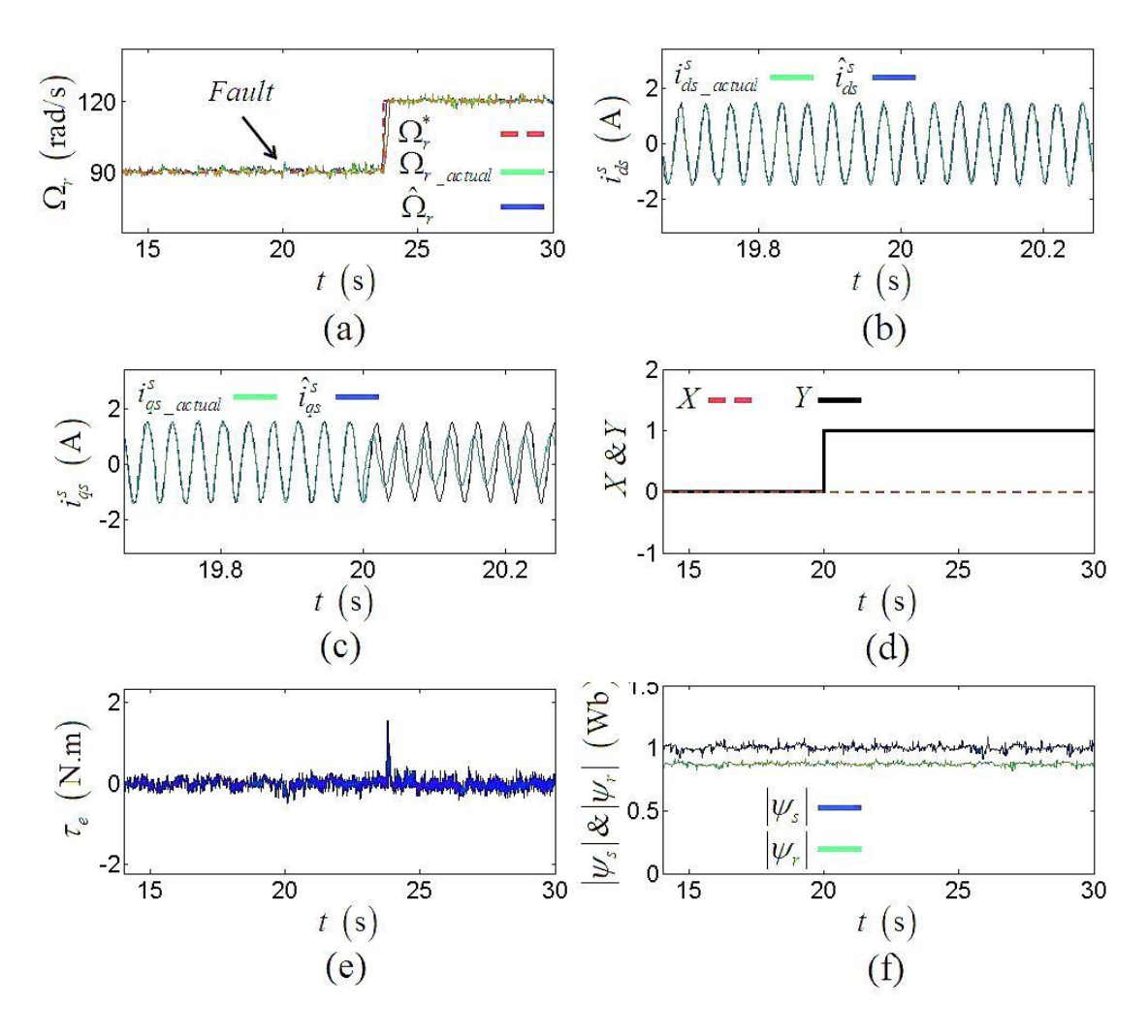


Figure 12: Performance of the proposed FTC strategy during no-load condition when a-phase sensor is healthy and b-phase sensor is faulty; (a) $\Omega_r^*, \hat{\Omega}_r, \Omega_{r_actual}$, (b) i_{ds}^s , (c)

$$i_{qs}^{s}$$
 , (d) $X \& Y$, (e) τ_{e} , (f) $\left|\psi_{s}\right| \& \left|\psi_{r}\right|$

Figure 13 shows experimental results of the suggested FTC strategy during post-fault operation. In this case, the three-phase IM drive system starts with both healthy current sensors and *b*-phase current sensor information is assumed to be lost. In Figure 13, before t=19.27 s, the drive system is under no-load condition, and after t=19.27 s, the load torque is equal to 3 N.m (59 % of the nominal load). In addition, the reference speed is 150 rad/s and $|\psi_s^*|$ =1 Wb.

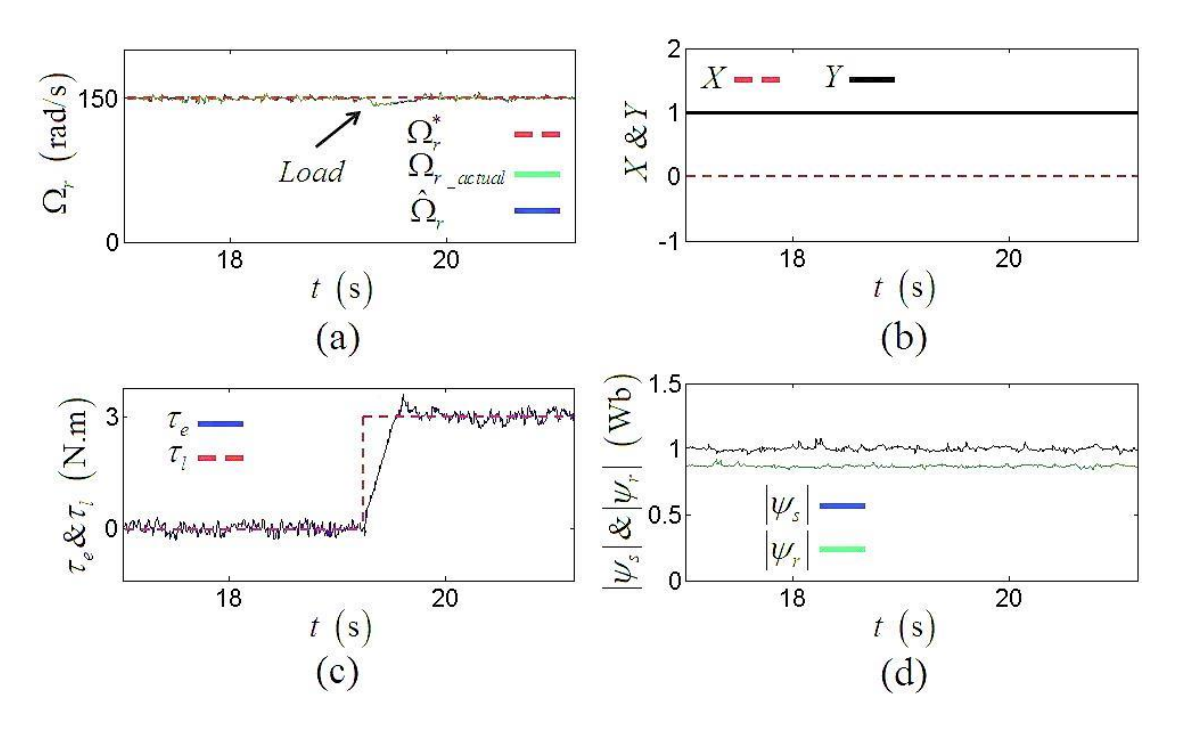


Figure 13: Performance of the proposed FTC strategy during load condition when a-phase sensor is healthy and b-phase sensor is faulty; (a) $\Omega_r^*, \hat{\Omega}_r, \Omega_{r_actual}$, (b)

$$X \& Y$$
, (c) $\tau_e \& \tau_l$, (d) $|\psi_s| \& |\psi_r|$

Figure 13(a) and Figure 13(d) illustrate uninterrupted and continuous speed and fluxes tracking performances under this scenario. The values of X and Y during post-fault mode are depicted in Figure 13(b). The X and Y statuses show that a-phase sensor is healthy and b-phase sensor is faulty. The estimated q-axis current and the actual d-axis current are utilized based on the X and Y values. As seen from Figure 13(c), the torque response of the three-phase IM has reasonable ripples (0.35 N.m) compared to the previous scenarios and its average value after the mechanical load is equal to the applied load.

7.4 Comparison between the proposed FTC strategy in this paper and the presented FTC strategy in [22] when a-phase sensor is healthy and b-phase sensor is faulty

Figure 14 displays the comparison of the torque response between the proposed FTC strategy in this paper and the presented FTC strategy in [22] aster the CSF. In both tests, *a*-phase sensor is healthy and *b*-phase sensor is faulty. In addition, to have a fair

comparison in both tests an encoder was used for the speed measurement. In Figure 14, the reference speed is 140 rad/s, $\tau_l = 0$ N.m and $|\psi_s^*| = 1$ Wb.

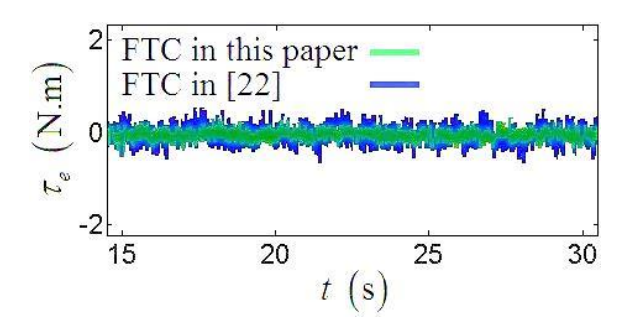


Figure 14: Comparison between the proposed FTC strategy in this paper and the presented FTC strategy in [22] when *a*-phase sensor is healthy and *b*-phase sensor is faulty

As shown, the average values of the torques are close to zero for both two experiments. As can be clearly seen, the MPTC in this paper outperforms the presented DTC system in [22] in terms of steady-state torque ripple. In addition, in the proposed FTC strategy in this paper the speed encoder is not needed while in the presented FTC strategy in [22] the speed encoder is needed.

8. CONCLUSION

This research has presented an implementation of a FTC strategy for encoderless MPTC of a three-phase IM drive against single-phase current sensor failure. The used control system is based on modifications of the MPTC strategy. For the detection and isolation of the faulty sensor, a TD and logic circuit module are used. In the suggested FTC scheme, the rotor speed estimation is based on the conventional rotor flux based MRAS algorithm and the stator currents are estimated using a flux observer. Through the flux observer, not only the stator currents but also the stator and rotor fluxes which are utilized in the modified MPTC strategy are estimated. The proposed FTC technique does not need an extra sensor and noticeable changes in the control system structure during post-fault operation. Extensive experimental results have shown that the three-phase IM drive system is able to detect and isolate the CSF and switch to the corresponding post-fault control strategy. The proposed encoderless FTC method works satisfactorily during different operation conditions such as normal, faulty, and load conditions.

As shown in this paper, the MRAS algorithm was used to estimate the motor speed. Nevertheless, this algorithm can be easily polluted by noises. To solve this problem, an EKF can be developed in the suggested encoderless MPTC method. The parameters dependency is one main drawback of the suggested control. This issue degrades the performance of the drive system. In future work, the motor parameters such as resistances in the proposed control system will be estimated during different operating conditions.

APPENDIX A

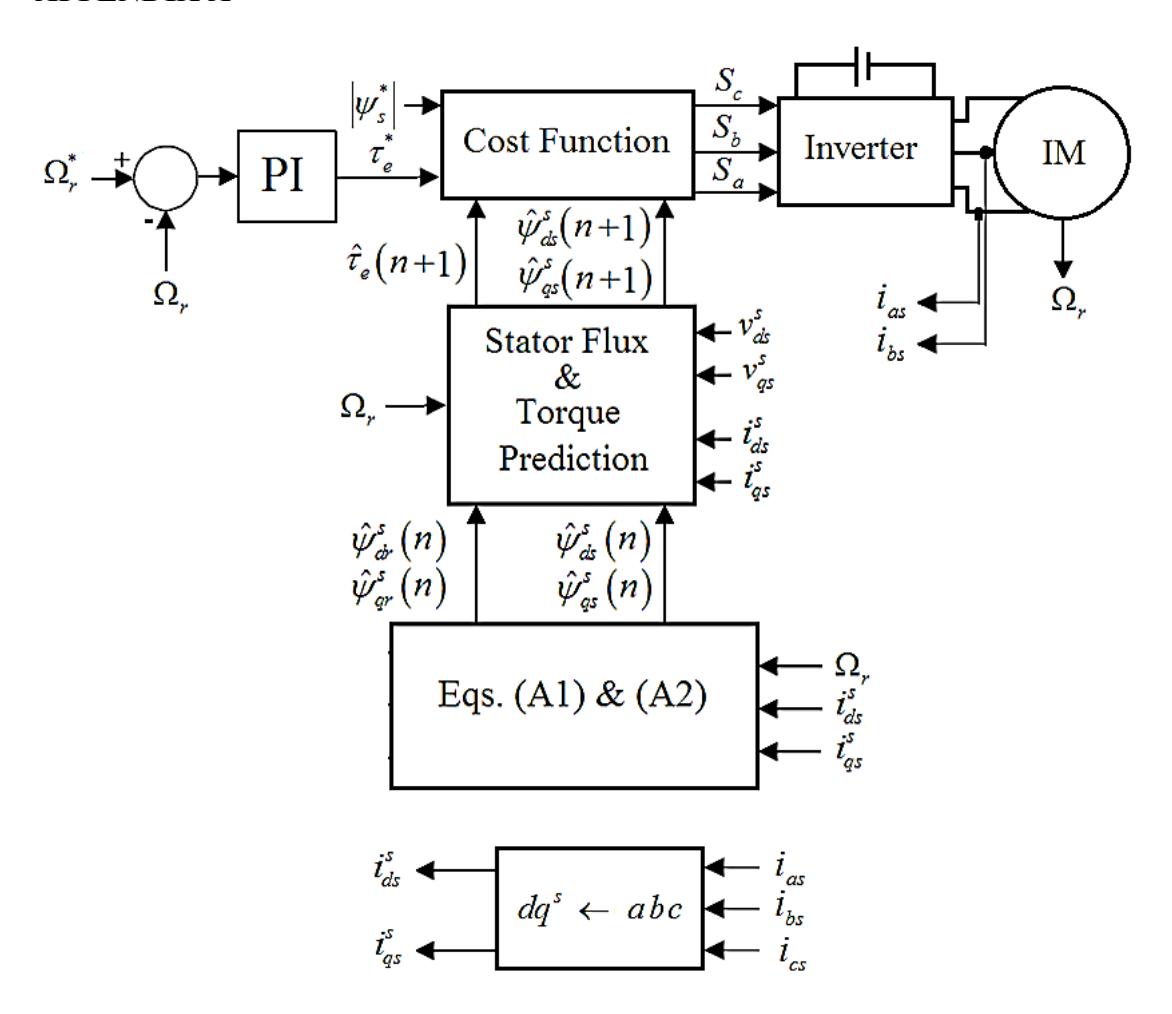


Figure A1: Schematic diagram of the conventional MPTC

In Figure A1:

$$\frac{d}{dt} \begin{bmatrix} \hat{\psi}_{dr}^{s} \\ \hat{\psi}_{qr}^{s} \end{bmatrix} = \frac{r_{r} L_{m}}{L_{r}} \begin{bmatrix} i_{ds}^{s} \\ i_{ds}^{s} \end{bmatrix} - \begin{bmatrix} \frac{r_{r}}{L_{r}} & \Omega_{r} \\ -\Omega_{r} & \frac{r_{r}}{L_{r}} \end{bmatrix} \begin{bmatrix} \hat{\psi}_{dr}^{s} \\ \hat{\psi}_{qr}^{s} \end{bmatrix} \tag{A1}$$

$$\begin{bmatrix} \hat{\psi}_{dr}^{s} \\ \hat{\psi}_{qr}^{s} \end{bmatrix} = \begin{bmatrix} L_{m} - \frac{L_{s}L_{r}}{L_{m}} & 0 \\ 0 & L_{m} - \frac{L_{s}L_{r}}{L_{m}} \end{bmatrix} \begin{bmatrix} i_{ds}^{s} \\ i_{qs}^{s} \end{bmatrix} + \begin{bmatrix} \frac{L_{r}}{L_{m}} & 0 \\ 0 & \frac{L_{r}}{L_{m}} \end{bmatrix} \begin{bmatrix} \hat{\psi}_{ds}^{s} \\ \hat{\psi}_{qs}^{s} \end{bmatrix}$$
(A2)

APPENDIX B

Table B1: Parameters of the three-phase IM

J		В		L_s, L_r		L_m		r_s		r_r
0.016 kg	$g.m^2$	0.001	N.m.s	0.61 H 0.6 H 10		10.45 Ω		14.65 Ω		
P	Nominal		Nominal		Nominal		N	ominal		Nominal
	torque		speed		voltage		power			frequency
4	5.1 N.m		148.1 r	ad/s	38	380 V		0.75 kW		50 Hz

Table B2: Controller and inverter parameters

							Inverter	
Dead	Sampling	2	K_p (speed	K_i (speed	K_p	K_i	type:	Switching
time	time	λ_{ψ}	controller)	controller)	(MRAS)	(MRAS)	2-level	frequency:
2 μs	50 μs	3	70	540	7	3	IGBT	variable
							inverter	

REFERENCES

- [1] Hajary A, Kianinezhad R, Seifossadat S G, Mortazavi S S, Saffarian A. Detection and localization of open-phase fault in three-phase induction motor drives using second order rotational park transformation. IEEE Transactions on Power Electronics. 2019;34(11):11241-11252.
- [2] Adamczyk M, Orlowska-Kowalska T. Postfault Direct Field-Oriented Control of Induction Motor Drive Using Adaptive Virtual Current Sensor. IEEE Transactions on Industrial Electronics. 2021;69(4):3418-3427.
- [3] Hannan M A, Ali J A, Mohamed A, Hussain A. Optimization techniques to enhance the performance of induction motor drives: A review. Renewable and Sustainable Energy Reviews. 2018;81:1611-1626.
- [4] Wang H, Yang Y, Ge X, Zuo Y, Yue Y, Li S. PLL-and FLL-Based Speed Estimation Schemes for Speed-Sensorless Control of Induction Motor Drives: Review and New Attempts. IEEE Transactions on Power Electronics. 2021.

- [5] Chen J, Huang J, Sun Y. Resistances and speed estimation in sensorless induction motor drives using a model with known regressors. IEEE Transactions on Industrial Electronics. 2018;66(4):2659-2667.
- [6] Rai R, Shukla S, Singh B. Sensorless field oriented SMCC based integral sliding mode for solar PV based induction motor drive for water pumping. IEEE Transactions on Industry Applications. 2020;56(5):5056-5064.
- [7] Zbede Y B, Gadoue S M, Atkinson D J. Model predictive MRAS estimator for sensorless induction motor drives. IEEE Transactions on Industrial Electronics. 2016;63(6):3511-3521.
- [8] Sun W, Xu D, Jiang D. Observability analysis for speed sensorless induction motor drives with and without virtual voltage injection. IEEE Transactions on Power Electronics. 2018;34(9):9236-9246.
- [9] Habibullah M, Lu D D C. A speed-sensorless FS-PTC of induction motors using extended Kalman filters. IEEE Transactions on Industrial Electronics. 2015;62(11):6765-6778.
- [10] Zhou D, Zhao J, Liu Y. Predictive torque control scheme for three-phase four-switch inverter-fed induction motor drives with DC-link voltages offset suppression. IEEE Transactions on Power Electronics. 2014;30(6):3309-3318.
- [11] Bindal R K, Kaur I. Torque ripple reduction of induction motor using dynamic fuzzy prediction direct torque control. ISA transactions. 2020;99:322-338.
- [12] Yan L, Dou M, Zhang H, Hua Z. Speed-sensorless dual reference frame predictive torque control for induction machines. IEEE Transactions on Power Electronics. 2019;34(12):12285-12295.
- [13] Bhowate A, Aware M, Sharma S. Predictive torque control with online weighting factor computation technique to improve performance of induction motor drive in low speed region. IEEE Access. 2019;7:42309-42321.
- [14] Amin A A, Hasan K M. A review of fault tolerant control systems: advancements and applications. Measurement. 2019;143:58-68.
- [15] Jankowska K, Dybkowski M. Design and Analysis of Current Sensor Fault Detection Mechanisms for PMSM Drives Based on Neural Networks. Designs. 2022;6(1):1-20.
- [16] Li H, Monti A, Ponci F. A fuzzy-based sensor validation strategy for AC motor drives. IEEE Transactions on Industrial Informatics. 2012;8(4):839-848.
- [17] Yu Y, Zhao Y, Wang B, Huang X, Xu D. Current sensor fault diagnosis and tolerant control for VSI-based induction motor drives. IEEE Transactions on Power Electronics. 2017;33(5):4238-4248.
- [18] Chakraborty C, Verma V. Speed and current sensor fault detection and isolation technique for induction motor drive using axes transformation. IEEE Transactions on Industrial Electronics. 2014;62(3):1943-1954.

- [19] Liu Y, Stettenbenz M, Bazzi A M. Smooth fault-tolerant control of induction motor drives with sensor failures. IEEE Transactions on Power Electronics. 2018;34(4):3544-3552.
- [20] Tabbache B, Rizoug N, Benbouzid M E H, Kheloui A. A control reconfiguration strategy for post-sensor FTC in induction motor-based EVs. IEEE transactions on vehicular technology. 2012;62(3):965-971.
- [21] Lu J, Zhang X, Hu Y, Liu J, Gan C, Wang Z. Independent phase current reconstruction strategy for IPMSM sensorless control without using null switching states. IEEE Transactions on Industrial Electronics. 2017;65(6):4492-4502.
- [22] Manohar M, Das S. Current sensor fault-tolerant control for direct torque control of induction motor drive using flux-linkage observer. IEEE Transactions on Industrial Informatics. 2017;13(6):2824-2833.
- [23] Zhang X, Foo G, Vilathgamuwa M D, Tseng K J, Bhangu B S, Gajanayake C. Sensor fault detection, isolation and system reconfiguration based on extended Kalman filter for induction motor drives. IET Electric Power Applications. 2013;7(7):607-617.
- [24] Zhang G, Zhou H, Wang G, Li C, Xu D. Current Sensor Fault-Tolerant Control for Encoderless IPMSM Drives Based on Current Space Vector Error Reconstruction. IEEE Journal of Emerging and Selected Topics in Power Electronics. 2019;8(4):3658-3668.
- [25] Wu C, Guo C, Xie Z, Ni F, Liu H. A signal-based fault detection and tolerance control method of current sensor for PMSM drive. IEEE Transactions on Industrial Electronics. 2018;65(12):9646-9657.
- [26] Fan S K S, Hsu C Y, Tsai D M, He F, Cheng C C. Data-driven approach for fault detection and diagnostic in semiconductor manufacturing. IEEE Transactions on Automation Science and Engineering. 2020;17(4):1925-1936.
- [27] Capolino G A, Antonino-Daviu J A, Riera-Guasp M. Modern diagnostics techniques for electrical machines, power electronics, and drives. IEEE Transactions on Industrial Electronics. 2015;62(3):1738-1745.
- [28] Salmasi F R, Najafabadi T A. An adaptive observer with online rotor and stator resistance estimation for induction motors with one phase current sensor. IEEE Transactions on Energy Conversion. 2011;26(3):959-966.
- [29] Wang W, Lu Z, Feng Y, Tian W, Hua W, Wang Z, Cheng M. Coupled fault-tolerant control of primary permanent-magnet linear motor traction systems for subway applications. IEEE Transactions on Power Electronics. 2020;36(3):3408-3421.
- [30] Wang G, Hao X, Zhao N, Zhang G, Xu D. Current sensor fault-tolerant control strategy for encoderless PMSM drives based on single sliding mode observer. IEEE Transactions on Transportation Electrification. 2020;6(2):679-689.

- [31] Cortes P, Rodriguez J, Silva C, Flores A. Delay compensation in model predictive current control of a three-phase inverter. IEEE Transactions on Industrial Electronics. 2011;59(2):1323-1325.
- [32] Bose B K. Power electronics and AC drives. Englewood Cliffs. 1986.
- [33] Kang Y C, Ok S H, Kang S H. A CT saturation detection algorithm. IEEE Transactions on Power Delivery. 2004;19(1):78-85.
- [34] Reza C M F S, Islam M D, Mekhilef S. A review of reliable and energy efficient direct torque controlled induction motor drives. Renewable and Sustainable Energy Reviews. 2014;37:919-932.
- [35] Prabhakar K K, Chinthakunta U R, Singh A K, Kumar P. Efficiency and performance analysis of DTC-based IM drivetrain using variable dc-link voltage for electric vehicle applications. IET Electrical Systems in Transportation. 2018;8(3):205-2014.
- [36] Luo C, Wang B, Yu Y, Chen C, Huo Z, Xu D. Decoupled stator resistance estimation for speed-sensorless induction motor drives considering speed and load torque variations. IEEE Journal of Emerging and Selected Topics in Power Electronics. 2019;8(2):1193-1207.
- [37] Kwon C K, Kim D S. Efficiency study at light load operation for AQDM based Adaptive MTPA Control for IM drive. In 2017 IEEE Transportation Electrification Conference and Expo (ITEC). 2017:5-8.
- [38] Morawiec M, Kroplewski P, Odeh C. Nonadaptive Rotor Speed Estimation of Induction Machine in an Adaptive Full-Order Observer. IEEE Transactions on Industrial Electronics. 2021;69(3):2333-2344.